Scientific Reports

https://doi.org/10.1038/s41598-026-52667-5

Article in Press

Glucose coated FeO@Fe_3O_4 nanoparticles show tunable catalytic reactivity and safety in a 3D hepatic in vitro model

Received: 29 December 2025

Accepted: 6 May 2026

Published online: 12 May 2026

Cite this article as: Morales Ovalle M.A., Rozman I., Winkler E.L. *et al.* Glucose coated FeO@Fe_3O_4 nanoparticles show tunable catalytic reactivity and safety in a 3D hepatic in vitro model. *Sci Rep* (2026). https://doi.org/10.1038/s41598-026-52667-5

Marco A. Morales Ovalle, Iza Rozman, Elin L. Winkler, Enio Lima Jr., Alja Štern, Katja Kološa, Bojana Žegura & Gerardo F. Goya

Glucose coated $FeO@Fe_3O_4$ nanoparticles show tunable catalytic reactivity and safety in a 3D hepatic *in vitro* model.

Marco A. Morales Ovalle[a,b,c,d,e#], Iza Rozman[f,g#], Elin L. Winkler[a,b,c], Enio Lima Jr.[a,b], Alja Štern[f,g], Katja Kološa[f], Bojana Žegura[f,g], and Gerardo F. Goya[d,e*]

[a] *Departamento de Magnetismo y Materiales Magnéticos, Gerencia de Física, Centro Atómico Bariloche, S. C. de Bariloche, 8400, Argentina*

[b] *Instituto de Nanociencia y Nanotecnología, CNEA/CONICET, Centro Atómico Bariloche, S. C. Bariloche, 8400, Argentina*

[c] *Instituto Balseiro, UNCuyo/CNEA, Centro Atómico Bariloche, S. C. Bariloche, 8400, Argentina*

[d] *Departamento de Fisica de la Materia Condensada, Universidad de Zaragoza, Zaragoza, Spain*

[e] *Instituto de Nanociencia y Materiales de Aragón, CSIC-Universidad de Zaragoza, Zaragoza, Spain*

[f] *National Institute of Biology, Department of Genetic Toxicology and Cancer Biology, Ljubljana, Slovenia.*

[g] *Biotechnical Faculty, University of Ljubljana, Slovenia*

*Correspondence: goya@unizar.es

[#] These authors contributed equally to this work.

Abstract

Iron-oxide magnetic nanoparticles (MNPs) have been extensively investigated as magnetically actable nanocatalysts for diagnostic and therapeutic applications. However, because wüstite/magnetite/maghemite phases can interconvert, coexisting Fe^{2+}/Fe^{3+} species may redirect Fenton-like chemistry and generate reactive oxygen species (ROS) profiles that differ from the intended biocatalytic pathway. Here we investigate monodisperse biphasic $FeO@Fe_3O_4$ core-shell MNPs with average particle size ⟨d⟩ = 9.6(5) nm, and their glucose-coated analogue, combining EPR radical analysis with toxicity testing in a 3D HepG2 hepatic spheroid model. Naked particles exhibited conventional Fenton-like behavior dominated by hydroxyl radicals (•OH), whereas glucose coating markedly suppressed •OH while increasing hydroperoxyl radicals (•OOH; ≈55 pM at 60 min), demonstrating ligand-controlled rerouting of the radical pathway. TEM mapping across spheroid cross-sections showed preferential MNP accumulation in the outer layer, with most observed events confined to the outer □10-15 mm, corresponding to an approximately one-cell-thick rim; sparse deeper events were observed up to □30-35 mm. MNPs produced dose- and time-dependent cytotoxicity in HepG2 spheroids, with IC_{50} values of 29.3 (24 h) and 10.8 (96 h) $mg \cdot cm^{-2}$, without evidence of lipid peroxidation or genotoxicity. MDA levels remained unchanged, the comet assay showed no increase in DNA damage, and gH2AX and phospho-H3 (p-H3) positive events were not detected. Our results show that glucose functionalization provides a simple route to modulate radical

pathways and define operational windows for redox-active FeO@Fe_3O_4 nano-reactors in oxidative nanomedicine.

Keywords: iron-oxide nanoparticles, Fenton-like catalysis, cytotoxicity, genotoxicity, HepG2 spheroids

Introduction

An increasing number of targeted therapies with innovative strategies for cancer treatments are based on the ability of magnetic nanoparticles (MNPs) to be remotely actuated by magnetic fields.[1,2] This physical property and their tunable surface chemistry make them particularly suitable for biomedical applications.[3–5] Thus, oncology strategies are seeking for such systems, adequately optimized, that could exploit both an efficient magnetic actuation and a controllable redox reactivity at the tumor interface.[6] Previous reports on MNPs capable of maintaining the Fe^{2+}/Fe^{3+} cycle to catalyze peroxide activation Fenton-like pathways in acidic, H_2O_2-enriched microenvironments characteristic of many solid tumors have already shown partial success.[7] Despite their promise for biotechnological applications, it is increasingly evident that current MNPs remain suboptimal in atomic-level design control,[8] and that a more rigorous understanding of their interactions with biological systems (together with comprehensive safety evaluation) is still required.[9]

Conversely, in other bio-based applications, the very same generation of reactive oxygen species (ROS) by certain iron-oxide phases is problematic, since oxidative stress and enzyme-like reactivity can introduce off-target biological effects and compromise the intended functionality.[10,11] The diverse surface reactivities of several iron oxide phases commonly used in biomedical

applications, such as magnetite Fe_3O_4 and maghemite g-Fe_2O_3 (and, less frequently, wüstite FeO) makes it difficult to predict their type of behavior in biological media.[12–15] These oxides can show a different catalytic role in Fenton-like reactions and, consequently, in their ROS generation capacity and biological impact.[16] Understanding how specific iron oxide phases and their combinations affect these properties is essential for defining their potential toxicity.

In this study, we engineered glucose-coated FeO@Fe_3O_4 core-shell nanoparticles aiming at a system with a coupled electron-rich (wüstite) core with a magnetite shell, creating a biphasic architecture that simultaneously enhances magnetic responsiveness and surface redox activity. By integrating thorough physicochemical insight with evaluation of their potential (geno)toxic effects in a three-dimensional (3D) human hepatic cell model prepared from the HepG2 cell line, we establish direct links between nanoscale structure, controlled •OOH radical generation, and their biological effects *in vitro*. Our findings position biphasic magnetic nanoparticles as tunable, remotely activatable oxidative nano-effectors for precision therapeutic applications.

Materials and Methods

Reagents

Iron(III) acetylacetonate ($Fe(acac)_3$, 97%), oleic acid (analytical standard), and trioctylamine (98%) were used for nanoparticle synthesis. Toluene (≥99.5%) and acetone (≥99.5%) were used for washing and dispersion. Anhydrous glucose (99.8%) and ammonium hydroxide solution (27% w/w) were employed

for the coating step. Unless otherwise stated, chemicals were purchased from Sigma-Aldrich (Merck) and used as received without further purification. Dulbecco's phosphate-buffered saline (DPBS) 10× (Gibco) was diluted to 1× with sterile water and used for washing coated nanoparticles; sterile water was also used for the final resuspension. For spin-trapping assays, EPR-grade 5,5-dimethyl-1-pyrroline N-oxide (DMPO, ≥97%; Sigma-Aldrich) served as the spin trap. Ultrapure water (Milli-Q, 18.2 MΩ·cm) and a 10 mM acetate buffer adjusted to pH 5 were used as dispersion media in these experiments. MEM medium (MEM-10370-046) and Fetal Bovine Serum (FBS, 10%) for cell culture and spheroid preparation were obtained from Gibco (Paisley, Scotland, UK). Sodium pyruvate (1 mM), L-glutamine (2 mM), penicillin/streptomycin (100 IU/mL), Non-Essential Amino Acids (NEAA) and methylcellulose were purchased from Sigma-Aldrich (St. Louis, MO, USA). The CellTiter-Glo® Luminescent Cell Viability Assay for the cytotoxicity evaluation was acquired from Promega (Madison, WI, USA) to quantify ATP levels. Dimethyl sulfoxide (DMSO) was obtained from Sigma Aldrich (Missouri, U. S.) and used as a positive control. The Lipid Peroxidation (MDA) Assay Kit for the MDA assay was obtained from Abcam (Cambridge, UK) to measure lipid peroxidation. tert-Butyl hydroperoxide (tBOOH) was purchased from Micropolo (Maribor, Slovenia) and used as a positive control. For the preparation of single cell suspensions, Collagenase was obtained from Thermo Fisher Scientific (Waltham, Massachusetts, U.S.). GelRed nucleic acid stain was acquired from Biotium (USA) and used for slide analysis. Benzo[a]pyrene purchased from

Merck (New Jersey, U. S.), etoposide and colchicine (both purchased from Sigma, St. Louis, MO, USA) served as positive controls. Paraformaldehyde (PFA, 4%) for flow cytometry analysis was obtained from Merck (New Jersey, U. S.) and used for cell fixation. Bovine Serum Albumin (BSA, 1%) was obtained from Sigma (St. Louis, Missouri, U. S.) and used for antibody incubation. The following antibodies were acquired from Miltenyi Biotech (Germany): γH2AX pSer139-APC (130-123-256) and pH3-PE (130-105-700). REA controls (Miltenyi Biotech) were included for non-specific antibody binding assessment. Etoposide (1.7 µM) and colchicine (0.1 µM), purchased from ChemCruz (Dallas, U. S.) and Merck (New Jersey, U. S.), respectively, were used as positive controls.

Nanoparticle Synthesis

$FeO@Fe_3O_4$ nanoparticles were obtained by thermal decomposition of organometallic precursors in trioctylamine. Iron(III) acetylacetonate (1 mmol) and oleic acid (3 mmol) were dispersed in trioctylamine (15 mL) in a three-neck round-bottom flask under mechanical stirring. The mixture was heated under a nitrogen atmosphere (»3.7 $L \cdot min^{-1}$) from room temperature to 200 °C, with a temperature increase of 5 ± 2 $°C \cdot min^{-1}$,and from 200 °C to 350 °C, with a temperature increase of 18 ± 6 $°C \cdot min^{-1}$. A water-cooled Allihn condenser (see Figure S1) was used throughout. Upon reaching 350 °C, the heating mantle was removed, and the reaction was allowed to cool to room temperature. The crude product was a homogeneous black dispersion that was weakly magnetically responsive. To collect the as-prepared material, the

resulting dark solution was treated with toluene and acetone in a 1:1:5 ratio in an Erlenmeyer flask to prevent solvent evaporation. A precipitate was obtained through magnetic decantation. Subsequently, the as-prepared precipitate was subjected to an organic excess removal protocol to obtain the labelled non-coated nanoparticles. The precipitate was repeatedly suspended in toluene, diluted in acetone, and magnetically precipitated; this cycle was performed until no further changes were observed in the FTIR spectra of the supernatant or the solid. It should be noted that while this process significantly reduces the organic layer to allow for aqueous interaction, trace amounts of hydrophobic residues remained on the nanoparticle surface. Samples of pure magnetite Fe_3O_4, used as control, were synthesized through the same route, but using different solvent and temperature profile (see Figures S3 and S4), as described in the Supplementary Material.

Glucose Coating Procedure

For the glucose coating procedure, non-coated $FeO@Fe_3O_4$ nanoparticles were suspended through sonication in a glucose-ammonium hydroxide solution at a 1:10 (w/v) ratio, which was prepared by dissolving anhydrous glucose in a 27% ammonium hydroxide solution (glucose mass being 5 times the initial nanoparticle weight). The mixture was then kept overnight with mechanical agitation. The entire coating process, including subsequent washing steps with PBS, was conducted under sterile conditions. Due to the excellent dispersion of the nanoparticles in water, recovery of the glucose-coated nanoparticles involved diluting the suspension in sterile PBS, centrifuging, and carefully

removing the supernatant while the pellet was held immobilized by a magnet. This washing process was repeated until a neutral pH was reached. Finally, the recovered glucose-coated nanoparticles were resuspended in 1500 µL of sterile water. The concentration of the final solution was determined gravimetrically by drying a known volume of the suspension at 75 °C and weighing the recovered nanoparticles.

Characterization of nanoparticles

Unless otherwise specified, XRD, TEM/SAED/HRTEM, and magnetic characterization were performed on the as-synthesized $FeO@Fe_3O_4$ nanoparticles before glucose coating. FTIR, SAXS, EPR, and all biological experiments were carried out using the glucose-coated material.

Crystallographic Structure

Structural characterization of the nanoparticles was performed using a Bruker D8 Advance powder X-ray diffractometer (Cu Ka, l=0.154 nm) at room temperature. Samples were prepared by depositing a concentrated MNP/acetone suspension onto a rounded glass substrate and allowing the solvent to evaporate completely, forming a tightly adhered dark powder layer.

Nanoparticle Morphology and Size

The morphology and size distribution of the nanoparticles were determined by TEM using a Tecnai T20 (Thermofisher) microscope operated at 200 kV and room temperature. TEM samples were prepared by applying a droplet of a low-concentration (translucent) nanoparticle suspension in toluene onto a carbon-coated copper grid and allowed to dry. A size histogram was obtained from

randomly labelled MNPs (using ImageJ 1.54f software), and the mean diameter and standard deviation were estimated by fitting a log-normal distribution.

Magnetic Properties

The magnetic properties of the nanoparticles were characterized using a S700X Superconducting Quantum Interference Device (SQUID) magnetometer (Quantum Design). Field-dependent magnetization (M vs. H) was measured at 300 K and at 90 K. The exchange bias effect signature was examined after cooling the sample from room temperature to 90 K in the presence of a 10 kOe applied field.

Surface Functionalization

Glucose coating effectiveness was evaluated through ATR-FTIR spectra, recorded at a spectral resolution of 4 cm^{-1} from 500 to 4000 cm^{-1} with a Spectrum Two spectrometer (PerkinElmer). In general, measurements were made by applying a droplet of a concentrated nanoparticle suspension in toluene or Milli-Q water directly onto the ATR crystal, and spectra were recorded as volatile substances evaporated.

Colloidal Properties

Size, polydispersity, and interparticle interactions of the glucose-coated nanoparticles in solution were measured using X-ray scattering at both Cu Kα and Mo Kα wavelengths on a Xenocs Xeuss 2.0 SAXS instrument. The data collected from these two sources were subsequently merged to provide a broader Q-range for analysis. The solution was contained in a 1.5 mm diameter borosilicate glass tube. Scattering Length Densities (SLDs) for the various

components were calculated using the NIST Center for Neutron Research (NCNR) scattering length density calculator, specifically for the Cu Kα source. These calculations were based on the known bulk densities of 5.41 g cm^{-3} for FeO, 5.17 g cm^{-3} for Fe_3O_4, 1.56 g cm^{-3} for glucose, and 1 g cm^{-3} for water. Data analysis and model fitting were performed using SasView 6.0.1 software.

Given the proximity in Scattering Length Densities (SLDs) of the FeO core (44.607×10^{-6} $Å^{-2}$) and Fe_3O_4 shell (40.452×10^{-6} $Å^{-2}$), as well as the low contrast between the glucose coating (14.170×10^{-6} $Å^{-2}$) and the aqueous solvent (9.469×10^{-6} $Å^{-2}$), the nanoparticles were approximated to "homogeneous" spheres with a weighted average SLD of 41.6985×10^{-6} $Å^{-2}$, based on the phase proportions estimated from XRD (ϕ_{core} ~0.3 and ϕ_{shell} ~0.7). All these SLDs were fixed during the whole fitting analysis. A fit to reveal the primary particle contributions was first performed over the Q-range from 5.040×10^{-2} to 4.837×10^{-1} A^{-1}. The distribution of radius from this initial result (0.0794(9)) was then fixed during the subsequent analysis, combining a sphere form factor and a square-well structure factor.

Free Radicals Detection and Quantification

For EPR, the non-coated FeO@Fe_3O_4 reference was evaluated only under acidic conditions (10 mM acetate buffer, pH 5). Water-condition EPR data are reported only for the glucose-coated nanoparticles and the corresponding nanoparticle-free control. The generation of DMPO adducts was determined at room temperature using an ELEXSYS II-E500 EPR spectrometer equipped with an X-band resonant cavity (9.4 GHz). Reaction mixtures for the EPR

experiments were prepared by dispersing 20 mL of glucose-coated $FeO@Fe_3O_4$ MNPs (2 mg/mL) in 20 mL of either a 10 mM pH 5 acetate buffer solution or Milli-Q water (for neutral pH conditions). This was followed by the addition of 10 mL of a DMPO/water solution (0.167 g/mL). The reaction was initiated by the addition of 2 mL of H_2O_2 30% (0.49 M). The solution was contained in a 1 mm diameter Q-band quartz tube. EPR spectra of each solution were recorded simultaneously with an MgO pattern crystal doped with a known concentration of Mn^{2+} attached to the tube, which served as an internal standard for DMPO adduct quantification. All spectra were processed using the Spin Fit software from Bruker. The baseline for each spectrum was computed with a 3rd-degree polynomial and then subtracted. Subsequently, the resonance lines were fitted using the hyperfine parameters of the identified components. The concentrations of DMPO adducts were then determined by comparing the fitted EPR spectrum area of each species with the area of the MgO/Mn^{2+} standard. For EPR, the non-coated $FeO@Fe_3O_4$ reference was evaluated only under acidic conditions (10 mM acetate buffer, pH 5). Water-condition EPR data are reported only for the glucose-coated nanoparticles and the corresponding nanoparticle-free control. In addition, the Fe_3O_4 control experiments (Figure S7 in Supplementary Material) were performed under the same spin-trapping EPR conditions used for $FeO@Fe_3O_4$, including the corresponding non-coated and glucose-coated Fe_3O_4 samples.

Assessment of (geno)toxicity *in vitro*

Cell Cultivation

The *in vitro* model of choice in our study was a 3D cell model (spheroids) derived from the human hepatocellular carcinoma cell line (HepG2) (ATCC HB-8065™, Manassas, VA, USA). Cells were grown in MEM medium supplemented with 10% FBS and 1 mM sodium pyruvate, 2 mM L-glutamine, 100 IU/mL penicillin/streptomycin, and NEAA, at 37 °C in a humidified atmosphere with 5% CO_2.

Spheroid Preparation

The spheroids were prepared using the force floating method as described by Štampar et al. [17]. Cell passages up to 13 were used. In brief, cells were seeded at a density of 3,000 cells per well into 96-well U-bottom plates (Corning Costar Corporation, New York, USA) using complete growth medium supplemented with 4% methylcellulose. The plates were centrifuged at 900 × g for 90 minutes to promote spheroid formation. The resulting spheroids were then incubated for 72 hours at 37 °C in a humidified atmosphere with 5% CO_2 to allow for maturation before experimentation.

Spheroids were exposed to FeO@Fe_3O_4 MNPs at concentrations ranging from 0.01 to 200 µg/mL, corresponding to 0.004 to 80 µg/cm². These concentrations refer to the mass of the whole MNPs. The range was selected based on the OECD Study Report and Preliminary Guidance on the Adaptation of the In Vitro Micronucleus Assay (OECD TG 487) for Testing of Manufactured Nanomaterials (September 2022).[18] Concentrations were calculated per surface area rather

than volume, as the tested $FeO@Fe_3O_4$ MNPs tend to settle onto the surface of the cells when in suspension.

Nanoparticle interaction with the cells in the spheroids – TEM

The study of the MNP's penetration into the 3D architecture of HepG2 spheroids was undertaken through a systematic analysis of sequential transmission electron microscopy (TEM) images along the cross section of the spheroids. After spheroids generated as described above and incubated with a MNPs concentration of 50 μg/mL were harvested, gently rinsed with phosphate-buffered saline (PBS, pH 7.4) to remove non-associated MNPs. The rinsed spheroids were chemically fixed in 2% glutaraldehyde in 0.1 M phosphate buffer (PB, pH 7.2) for 2 h at room temperature, followed by fixation in 1.5% glutaraldehyde in 0.05 M PB at 4 °C overnight. Samples were post-fixed with 1% osmium tetroxide for 1 h at room temperature, dehydrated through a graded ethanol series (30%, 50%, 70%, 90%, and 100%), and infiltrated with epoxy resin. For cross-sectional imaging, resin blocks were polymerized at 60 °C for 48 h, and ultrathin sections (~70 nm) were cut using an ultramicrotome. Sections were collected on copper grids and contrasted with 2% aqueous uranyl acetate and lead citrate. TEM imaging was carried out on a Tecnai T20 microscope (Thermo Fisher Scientific, USA) operating at 200 kV. For each condition at least three spheroids were analyzed. In addition, for one representative spheroid, a continuous linear montage was acquired across the section by collecting consecutive adjacent fields from one outer edge to the opposite border and stitching the images into a single composite.

Oxidative stress induction – MDA Assay

To check the degree of oxidative stress produced by the $FeO@Fe_3O_4$ MNPs, malondialdehyde (MDA) was used as a marker of lipid peroxidation. For this purpose, the Lipid Peroxidation (MDA) Assay Kit (Abcam, Cambridge, UK) was used. This kit measures lipid peroxidation by detecting MDA, which reacts with thiobarbituric acid (TBA) to form a colorimetric/fluorometric product, with intensity proportional to the MDA concentration in the sample. HepG2 spheroids were exposed to graded concentrations of $FeO@Fe_3O_4$ MNPs (2-20 $\mu g/cm^2$) for 4 and 24 hours. Evaluated concentrations were determined based on the results of the cell viability assay in a way that the highest tested concentration did not decrease cell viability by more than 25-30%. At each time point, spheroids were collected, rinsed with 1×PBS, and homogenized in MDA Lysis Buffer supplemented with BHT. The homogenates were centrifuged at 13,000 × g for 10 minutes, and the resulting supernatant was transferred to microcentrifuge tubes containing the TBA solution, prepared according to the manufacturer's instructions. Samples were then incubated at 95 °C for 60 minutes, followed by a 10-minute cooling period in an ice bath. Absorbance at 532 nm was measured using the BioTek Cytation 5 Cell Imaging Multimode Reader (Agilent, Santa Clara, USA). Each experimental condition was tested in triplicate, and the experiment was independently repeated three times. Negative (cell medium), solvent (up to 3% Milli-Q water), and positive (1 mM tBOOH) controls were included in all assays.

Cytotoxicity – measurement of the ATP content

The cytotoxicity of $FeO@Fe_3O_4$ MNPs was assessed using the CellTiter-Glo® Luminescent Cell Viability Assay. This homogeneous method quantifies ATP levels as an indicator of metabolically active, viable cells. HepG2 spheroids were exposed to varying concentrations of $FeO@Fe_3O_4$ MNPs (0.004–80 $\mu g/cm^2$) for 24 and 96 hours. The assay was carried out according to the manufacturer's instructions with slight modifications. Briefly, spheroids in 50 µL of culture medium were transferred to a white opaque 96-well plate, followed by the addition of 50 µL of CellTiter-Glo® reagent per well. The contents were mixed by pipetting to ensure complete cell lysis within the spheroids, and the plate was incubated for 20 minutes at room temperature. Luminescence was then measured using a luminometer (Synergy MX, BioTek, Winooski, VT, USA). Experiments were conducted in five replicates for each condition and repeated independently three times to ensure reproducibility. A negative (cell medium), a solvent (up to 3% Milli-Q water), and a positive control (15% DMSO), were included in the experiments. Significant differences in cell viability between exposed cells and the solvent control group (non-exposed cells) were analyzed using a One-Way Analysis of Variance (ANOVA) and Dunn's multiple comparison test in GraphPad Prism 10 (GraphPad Software, San Diego, CA, USA).

The Alkaline Comet Assay

DNA damage following exposure to $FeO@Fe_3O_4$ MNPs was assessed using the alkaline comet assay. HepG2 spheroids were exposed to graded non-cytotoxic

concentrations of MNPs (0.004–10 μg/cm^2) for 24 and 96 hours. After each exposure period, spheroids were dissociated into single-cell suspensions. Namely, spheroids were collected and washed with 1× PBS, then incubated with a mixture of collagenase , MEM, and TrypLE for 10 min (37 °C, 5% CO_2). Following enzymatic treatment, spheroids were further dissociated by gentle pipetting. Enzymatic activity was subsequently quenched by the addition of complete cell culture medium. The comet assay was performed according to the protocol described by Štampar et al.[17] and the conditions are detailed in Table S3 of the Supplementary Material. Slides were stained with GelRed nucleic acid stain (Biotium, USA) following the manufacturer's instructions, and comet scoring was carried out using a fluorescence microscope and Comet Assay IV software (Instem, Philadelphia, USA). Controls included negative control (cell culture medium), solvent control (up to 3% Milli-Q water), and positive controls (30 μM and 5 μM benzo[a]pyrene for 24 and 96-hour exposures, respectively). Each experiment was independently repeated three times, with 50 nuclei analyzed per experimental point. Statistical analysis was conducted in GraphPad Prism 10 using the Kruskal–Wallis nonparametric test, followed by Dunn's multiple comparison test to evaluate differences in tail DNA percentage between groups.

Analysis of γH2AX and p-H3 positive cells by flow cytometry

To further evaluate the potential genotoxic effects of FeO@Fe_3O_4 MNPs, phosphorylation of two histones – H2AX and H3 – was examined by flow cytometry. Phosphorylated histone H2Ax, forming γH2Ax, is a marker of

double-strand breaks (DSBs),[19] while phosphorylation of H3 (pH3) reflects mitotic cells and is a marker for exposure to aneugenes.[20] Three-day-old HepG2 spheroids were exposed to graded non-cytotoxic concentrations of MNPs (0.04–20 μg/cm^2) for 24 and 96 hours, after which they were dissociated into single-cell suspensions. The cells were washed twice with 1×PBS, fixed in 4% paraformaldehyde (PFA), and stored at 4 °C. Before analysis, cells were washed again with 1×PBS and incubated for 30 minutes in 1% BSA containing antibodies against γH2AX pSer139-APC (130-123-256) and pH3-PE (130-105-700), diluted 1:50. REA controls were included to account for non-specific antibody binding.

Etoposide (1.7 μM) and colchicine (0.1 μM) were used as positive controls, while fixed cells in complete growth medium and medium containing up to 3% Milli-Q water served as negative and solvent controls, respectively. The experiment was repeated three times independently. Samples were analyzed on a MACSQuant Analyzer 10 flow cytometer using MACSQuantify™ (Miltenyi Biotech, Germany) and FlowJo V10 (Becton Dickinson, New Jersey, USA). Statistical analysis was conducted using GraphPad Prism 10.

Results and Discussion

The FeO@Fe_3O_4 MNPs investigated here were intentionally engineered as redox-active, magnetically actable nano-reactors in which controlled ROS fluxes are desirable (e.g., as “oxidative nanomedicine” effectors). The FeO (Fe^{2+}-rich) core coupled to a Fe_3O_4 shell was selected to combine a local reservoir of Fe^{2+}/Fe^{3+} redox pairs that can sustain Fenton-like cycling in the

presence of different substrates. In parallel, the glucose coating was intended to deliberately probe whether a simple, biogenic ligand can tune the radical pathway (shifting the balance away from highly reactive •OH). Because these design choices target eventual biological use, as a first step in their potential applications we established both their physicochemical performance in ROS generation by EPR and also whether the resulting constructs operate within a safe biological window. The X-ray diffraction (XRD) pattern of the synthesized nanoparticles showed two distinct phases of iron oxides, wüstite (FeO, space group $Fm\bar{3}m$) and magnetite (Fe_3O_4, space group $Fd\bar{3}m$). Relative amounts of phases were 27% and 73% and estimated grain sizes of ~6.9 nm and ~2.4 nm, for FeO and Fe_3O_4, respectively. A quantitative refinement of these phases by the Rietveld method (Figure 1) was done using two models. In the first, no coupling between the phases was considered, and the lattice parameter of FeO (4.2079 Å) was found to be half of the lattice parameter of Fe_3O_4 (8.4050 Å). A second approach, with a coupling between the phases introduced in the refinement, yielded a shared microstrain parameter of ~0.25% (see Table S1 in Supplementary Material). These results indicate that the FeO@Fe_3O_4 MNPs are composed of two coupled phases, with Fe_3O_4 governing the overall crystalline framework, as inferred from the bulk lattice parameter (8.3941 Å).[21] The structural predominance of Fe_3O_4 results in a lattice distortion of the FeO component, whose parameter departs by 2.3% from the bulk value (4.301 Å).[22,23]

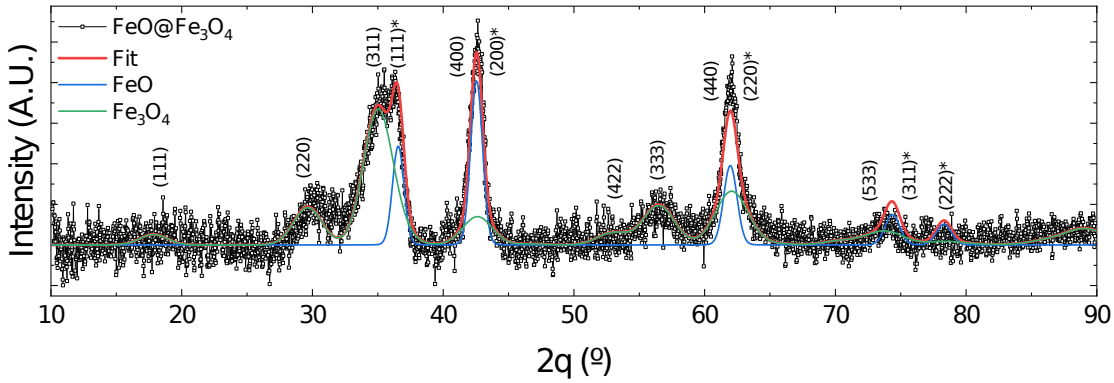

Figure 1. X-ray diffraction (XRD) pattern of synthesized FeO@Fe_3O_4 nanoparticles. The raw experimental data is shown in black. The Rietveld refinement fits for the wüstite (FeO) and magnetite (Fe_3O_4) phases are displayed in blue and green, respectively. The red line represents the combined Rietveld fit of both phases, showing its agreement with the raw data.*

Bright field TEM micrographs (Figure 2a) allowed for the determination of the morphology and size distribution of the synthesized MNPs. The size histogram, fitted with a log-normal function, yielded a mean diameter ⟨d⟩=9.6(5) nm; thus, the system can be considered as monodisperse (σ<10%). The determined value was consistent with the grain size estimated by Rietveld refinement when considering biphasic nanoparticles.

Electron diffraction patterns (Figure 2b) revealed rings indexed to an $Fm\bar{3}m$ structure, characterized of the FeO phase.[24] While the {111} reflections of the $Fd\bar{3}m$ structure (Fe_3O_4) identified in X-ray data[25] were not distinctly resolved in the selected area electron diffraction (SAED) patterns due to overlapping interplanar distances and the phase coupling suggested by Rietveld refinement, HRTEM provide two representative conditions to resolve the heterostructure: i) The core oriented in a Bragg condition (Figure 2c-d) displayed lattice fringes (2.4 Å) corresponding to the (111) planes of FeO, while the shell remained off-Bragg, allowing for an estimation of the core radius (~2.7 nm) and shell thickness (~2.7 nm) for an individual nanoparticle. In

contrast, oriented shell (Fe_3O_4) into Bragg condition (Figure 2e-f), lattice fringes (2.9 Å) corresponding to the (220) planes were resolved. These local structural observations confirmed the core-shell architecture, which is further validated by the magnetic exchange bias effect (Figure S2), a characteristic fingerprint of the ferrimagnetic-antiferromagnetic coupling at the Fe_3O_4/FeO interface.

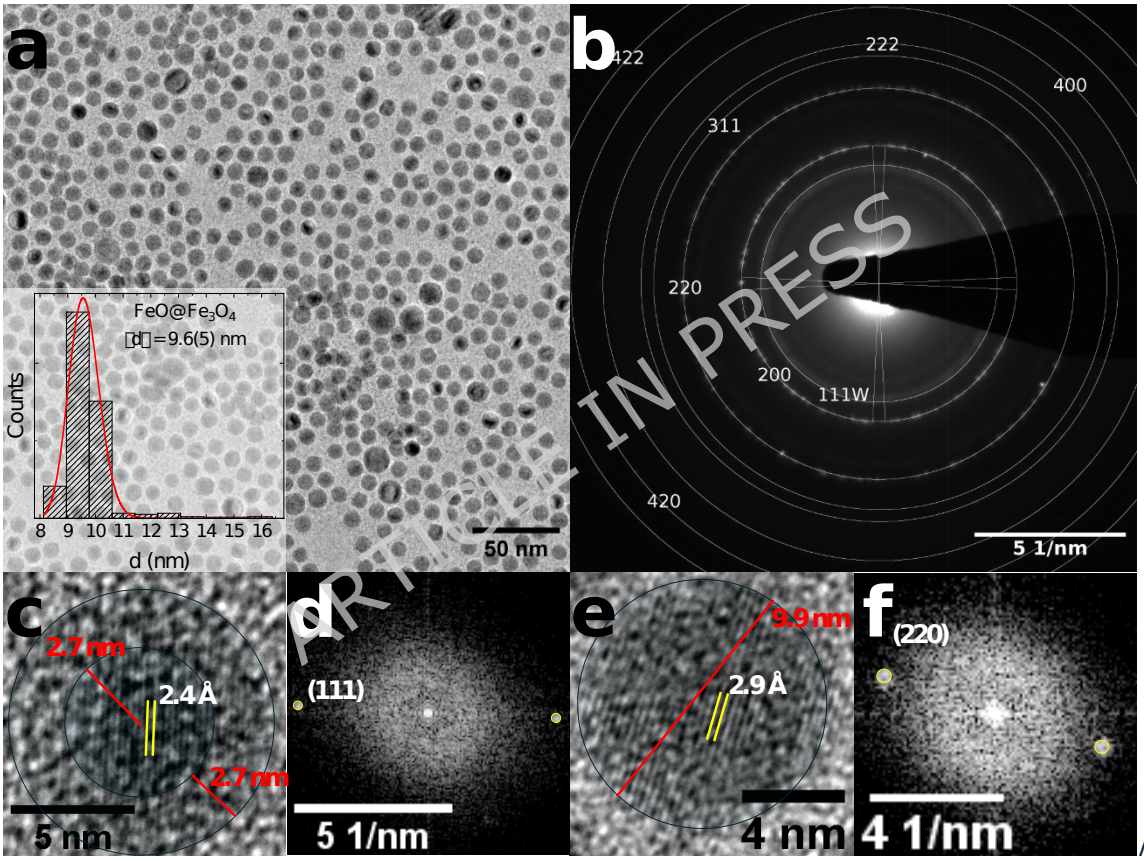

Figure 2. Transmission electron microscopy (TEM) characterization of synthesized FeO@Fe_3O_4 nanoparticles. Panel a: Bright-field TEM micrograph; the inset shows the size distribution histogram with a log-normal fit (9.6(5) nm). Panel B: Selected area electron diffraction (SAED) pattern with rings indexed to the $Fm\bar{3}m$ (FeO) and $Fd\bar{3}m$ (Fe_3O_4) phases. Panel c-d: HRTEM image (c) and corresponding FFT (d) of a single nanoparticle with core in Bragg condition, while the shell remains off-Bragg. Panel (e-f) HRTEM image (e) and corresponding FFT of a nanoparticle with the shell in Bragg condition (core off-Bragg).

Nanoparticle Coating

The presence of a glucose coating on the $FeO@Fe_3O_4$ MNPs after functionalization was assessed through Fourier Transform Infrared (FTIR) spectroscopy (Figure 3). The spectrum of the 'naked', non-coated MNPs taken for comparative purposes showed the characteristic C-H stretching vibrations at 2921 cm^{-1} and 2852 cm^{-1}, alongside a prominent 1538 cm^{-1} band indicative of surface-bound carboxylate from oleic acid,[26,27] as expected from the synthesis route. For the glucose-coated MNPs, the strong absorption band at 1012 cm^{-1} (C-O stretching) was evident, closely matching the corresponding band of pure glucose. This strong correlation of both spectra confirmed the attachment of glucose to the nanoparticle surface with good efficiency. Also, the C-H stretching vibrations in the 2900 cm^{-1} region could still be observed, probably associated with the glucose coating as evidenced by their similarity to the pure glucose spectrum. Moreover, the functionalized MNPs exhibited those additional absorption bands characteristic of glucose, including a very broad O-H stretching band centered around 3280 cm^{-1} and broader C-H stretching vibrations at 2923 cm^{-1} and 2854 cm^{-1}.[27] The broad absorption bands below 600 cm^{-1} could be assigned to the Fe-O stretching vibrations of the MNPs cores.[28]

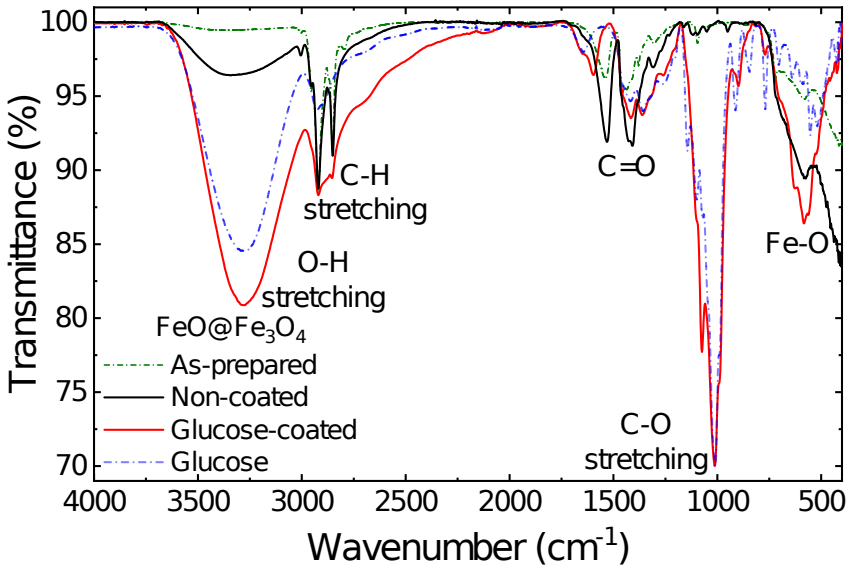

Figure 3. Fourier Transform Infrared (FTIR) spectra comparing non-coated and glucose-coated $FeO@Fe_3O_4$ nanoparticles. The non-coated $FeO@Fe_3O_4$ nanoparticles (black line) and after glucose coating (red line) were normalized to 2921 cm^{-1} C-H asymmetric stretching peak. The dark green and blue dashed lines *provide a reference spectrum of the* as-prepared nanoparticles *and* pure hydrated glucose*. The "non-coated" designation refers to particles that have undergone a cleaning procedure to remove the organic surfactant from "as-prepared" nanoparticles.*

Colloidal Properties

The size, polydispersity, and interparticle interactions of the glucose-coated $FeO@Fe_3O_4$ nanoparticles in solution were studied through Small-Angle X-ray Scattering (SAXS) (Figure S5). The fitting results yielded a mean radius ⟨d⟩=5.957(4) nm and polydispersity s=0.0794(9) when considering only a sphere form factor. Both parameters are consistent with the TEM-derived $FeO@Fe_3O_4$ mean diameter and polydispersity (σ<10%), suggesting a glucose shell thickness of about ~1.2 nm. However, the initial approach failed in the high-Q region, and fitting the full Q-range with many free parameters introduced strong correlations. Fixing the polydispersity from the sphere form-factor fit and using a square-well structure factor (parameters summarized in Table S2 of Supplementary Material) markedly improved the full-range fit, yielding a mean radius of 6.031(3) nm, still consistent with TEM and the initial

SAXS estimate. The resulting parameters also indicated an attractive interparticle interaction among the glucose-coated nanoparticles in solution, with well-width parameters, suggesting that this attraction extends for approximately 60% of the particle's radius beyond its surface.

EPR Evidence for Fenton-Like Radical Pathways

Spin-trapping EPR spectroscopy was performed to identify reactive oxygen species generated by glucose-coated $FeO@Fe_3O_4$ nanoparticles at pH 5 and in water, and by non-coated $FeO@Fe_3O_4$ nanoparticles at pH 5 (Figure S6 in the Supplementary Material). In the blank control (i.e., without nanoparticles), low concentrations of •OH radicals were observed, with negligible •OOH radicals (Figure 4B). As expected for Fenton-like reactions mediated by the Fe^{2+} ion, the non-coated nanoparticles led to a significant increase in •OH radical concentration, approaching 15 pM after 60 min.

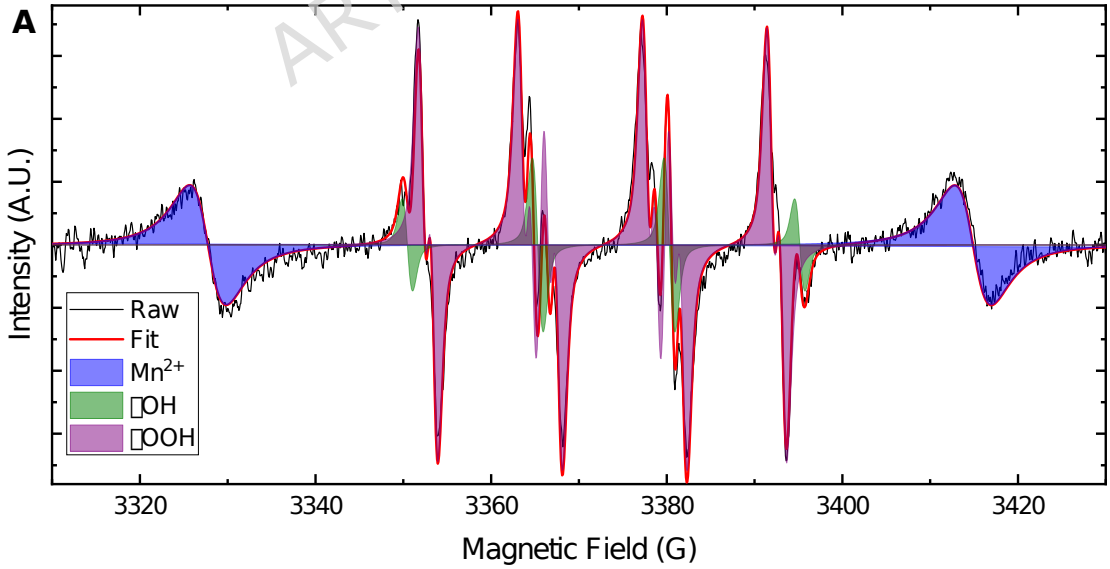

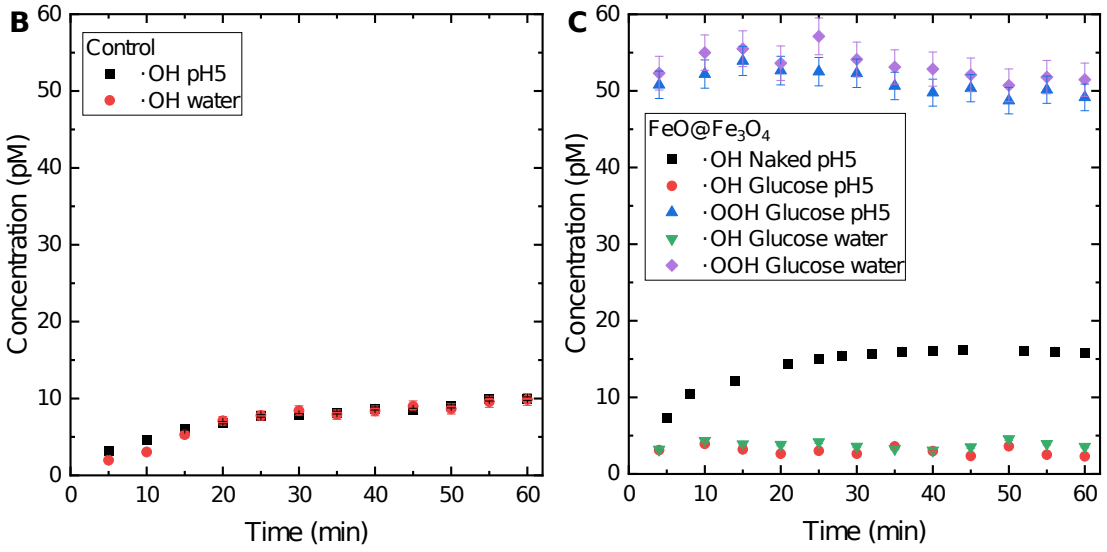

Figure 4. A: EPR spectrum (black line) of DMPO-adducts after exposure of the nanoparticles to H_2O_2 in water. The raw data is fitted (red line) to contributions from hydroxyl radicals (DMPO-•OH, green area) and hydroperoxyl radicals (DMPO-•OOH, violet area). A Mn^{2+} standard (blue area) is included for DMPO-adducts' quantification. The estimated concentration of hydroxyl and hydroperoxyl radicals as a function of time in the control (i.e., without nanoparticles) (B), and the time-dependent radical generation in nanoparticle-containing samples (C).

In contrast, the glucose-coated nanoparticles significantly suppressed the generation of •OH radicals (below 5 pM) and instead led to a sustained increase in the concentration of •OOH radicals (Figure 4C), reaching a peak of approximately 55 pM before slowly decaying over 60 min. These results suggest that the glucose coating is actively influencing the radical generation mechanism by acting as a scavenger of the highly reactive •OH radicals, promoting a dominant pathway towards the generation of •OOH species. For comparison, pure Fe_3O_4 nanoparticles of similar size and synthesis origin exhibit a predominant production of •OH radicals in their non-coated state (Figure S7 in the Supplementary Material); however, upon glucose coating, the radical output shirts toward •OOH, while maintaining the characteristic kinetics decay of magnetite.

The above data indicate that $FeO@Fe_3O_4$ MNPs are controllable oxidative nano-reactors. The coupled FeO/Fe_3O_4 biphasic architecture provides accessible Fe^{2+}/Fe^{3+} redox couples required for peroxide activation, whereas glucose functionalization strongly attenuates •OH and shifts the radical output toward •OOH. This effect may arise from ligand-mediated scavenging of surface-bound •OH and/or from a reduction in interfacial Fe-site accessibility, as commonly reported for coated iron-oxide nanozymes. This rerouting of radical speciation is relevant for biomedical use because •OH is highly reactive and diffusion-limited, whereas •OOH/$•O_2^-$ participates in longer-lived redox cycles. Moreover, the modest DMPO-adduct levels observed under our assay conditions are consistent with catalytic activity being retained while the most damaging radical channel is suppressed, in the absence of detectable lipid peroxidation and genotoxicity under the tested conditions.

Although the present study examined only glucose as the surface ligand, the rerouting of radical speciation is not expected to be unique to this molecule. In the case of glucose, the literature suggests that carbohydrate oxidation is promoted by •OH generated at Fe^{2+} sites, and that this oxidation is strongly reduced by the addition of •OH radical scavengers or Fe^{2+}-chelating agents.[29] This process involves the formation of a glucose peroxyl radical intermediate, which can subsequently release •OOH radicals into the solution[30]. More generally, surface ligands can alter peroxide access to Fe sites, modulate interfacial electron transfer, and scavenge short-lived radicals, thereby shifting the relative •OH/•OOH output. In this context, other coordinating or

hydrophilic ligands, such as carboxylates or polysaccharides, may also modify the radical pathway, although the direction and magnitude of the effect will depend on ligand binding strength, surface density, and redox activity. For instance, it has been reported that organic acids or alcohol groups can produce carbon-centered radicals in presence of •OH generated from Fe^{2+} sites.[31] Our data therefore support a ligand-dependent, rather than glucose-exclusive, control of radical speciation; systematic comparison among ligands lies beyond the scope of the present work.

Safety evaluation of $FeO@Fe_3O_4$ nanoparticles

Nanoparticle interaction with Spheroids

The MNP penetration's profile into 3D spheroids was assessed through a reconstruction from a sequential ~35–40 TEM images acquired along the spheroid cross-section was performed. A high-magnification reconstruction of an untreated control spheroid is provided in Figure S9 of the supplementary material to serve as a baseline for the intact spheroid architecture. Following 24-hour exposure to glucose-coated $FeO@Fe_3O_4$ MNPs, a low-magnification cross-section (~120 µm) of the exposed spheroid showed a clear preferential accumulation of NP clusters at the spheroid rim (Figure 5, upper panel). Higher-magnification images were then analyzed qualitatively to identify localization patterns in the examined sections. A major fraction of the MNPs was found forming clusters at the spheroid surface, consistent with the densely packed rim acting as a barrier to penetration (Figure 5d). However, also transcellular uptake with morphological alterations in the periphery was

observed (Figure 5a) and, within this region, MNPs were found confined to membrane-bound vesicles (endosomes), consistent with endocytosis. A main fraction of the internalized MNPs were detected distributed at 7-10 µm depth from the rim, defining the initial penetration zone. Deeper inside penetration was scarce (Figure 5b,c): few MNPs were observed at ≈10-15 µm (Figure 5c) and exceptionally at »30-35 µm (Figure 5b) from the rim. In Figure 5c, MNPs lie in intercellular spaces, indicative of paracellular transport, whereas in Figure 5b they appear in the cytosol without visible endosomal membranes, suggesting either non-endocytic entry or post-endocytic endosomal escape. The deepest penetration co-localizes with regions showing greater morphological damage, suggesting an association between MNP exposure and compromised cellular integrity.

From this single-spheroid dataset, we identify three modes of NP localization: (i) adsorption at the spheroid surface (rim), (ii) presence in intercellular clefts consistent with paracellular transport, and (iii) intracellular localization via transcellular uptake, the latter resolved into endosome-confined and cytosolic populations. The images also showed penetration to defined depths and a spatial co-occurrence between deeper NP presence and increased peripheral morphological damage, suggesting a possible association of these two effects. Considered together with the NP surface chemistry, the data are compatible with the hydrophilic glucose shell favoring interaction with the spheroid periphery and allowing both intercellular and intracellular localization. These TEM observations are qualitative and limited to the analyzed sections under a

single exposure condition; they describe localization patterns and penetration depths, but do not quantify the amount of nanoparticles internalized within spheroids or establish uptake efficiency at the population level. Although MNPs appear as clusters (consistent with SAXS indications of attractive interparticle interactions), the glucose coating likely reduces nonspecific protein fouling that would otherwise promote larger, immobilizing aggregates.[32]

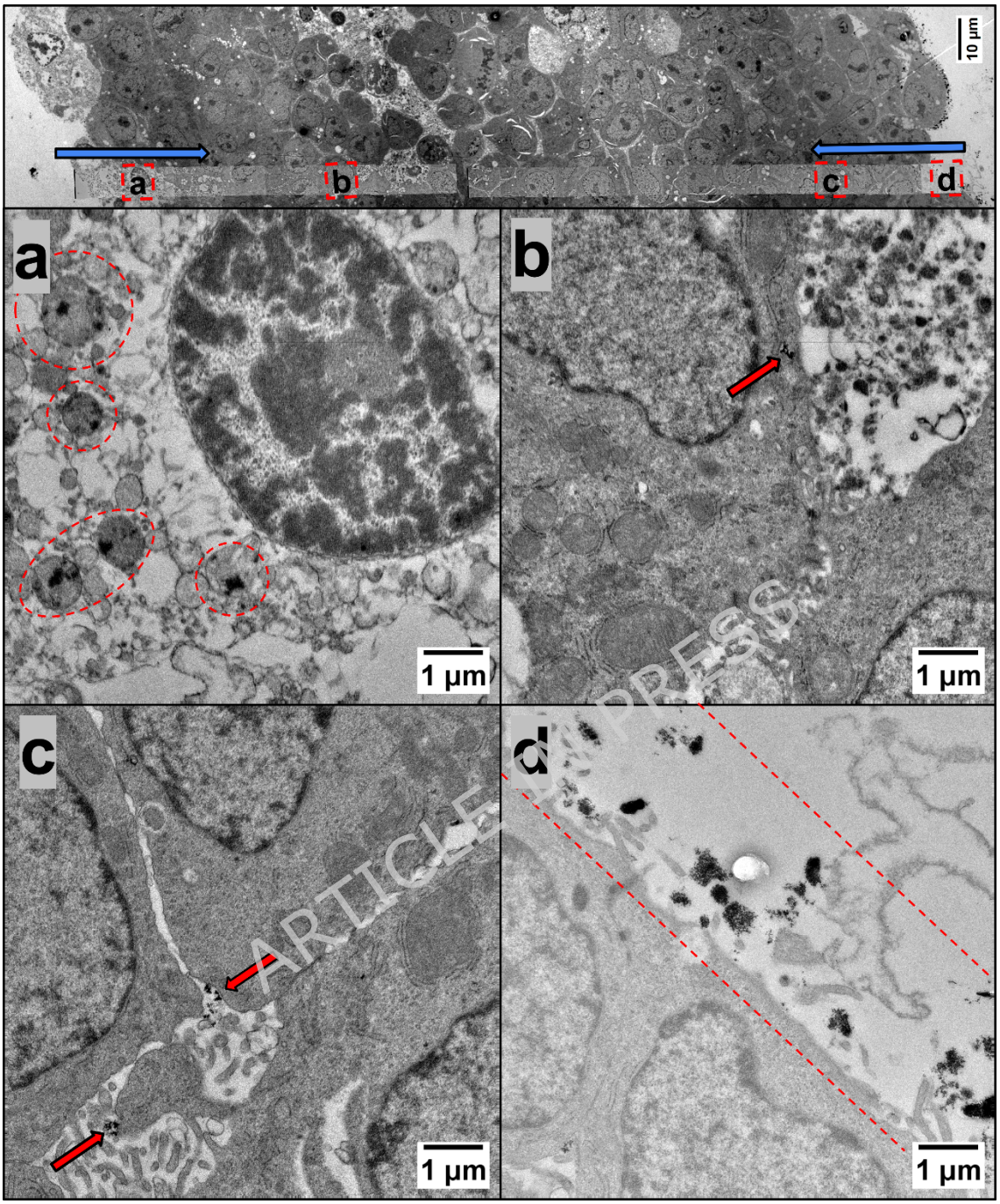

Figure 5. Transmission electron microscopy (TEM) images showing the qualitative localization of glucose-coated FeO@Fe_3O_4 nanoparticles across HepG2 spheroid cross-sections after 24 h exposure. The top panel provides a panoramic overview of the spheroid cross-section, with blue arrows indicating the outward-to-inward direction of MNP uptake. Panels a–d show higher-magnification regions in which nanoparticles were observed. Nanoparticles are highlighted by red dashed circles (a), red arrows (b, c), and red dashed lines (d).

Cyto and Genotoxiciy of the $FeO@Fe_3O_4$ nanoparticles

Potential adverse effects (cyto and genotoxicity) of $FeO@Fe_3O_4$ MNPs were evaluated using an advanced human hepatic *in vitro* model, HepG2 spheroids (Figure S8), which offers a compelling alternative to traditional monolayer cultures by enhancing cell–cell interactions and better preserving liver-specific functions, such as the expression of metabolic enzymes. As a result, it more closely mimics *in vivo* hepatic conditions.[33] Furthermore, the HepG2 cell line is widely used as an *in vitro* model for toxicological studies due to its expression of the wild-type p53 tumor suppressor protein and its retained activity of various xenobiotic-metabolizing enzymes.[34]

The cytotoxicity of the tested $FeO@Fe_3O_4$ MNPs was assessed using the CellTiter-Glo Assay. As shown in Figure 6, cell viability decreased in a dose- and time-dependent manner following 24 and 96 hours of exposure. Notably, after 96 hours, a more pronounced cytotoxic effect was observed even at lower concentrations, indicating increased sensitivity with prolonged exposure. Furthermore, after 24 hours of exposure, an IC_{50} value was 29.3 $\mu g/cm^2$, while after 96 hours the IC_{50} value decreased to approximately 10.8 $\mu g/cm^2$.

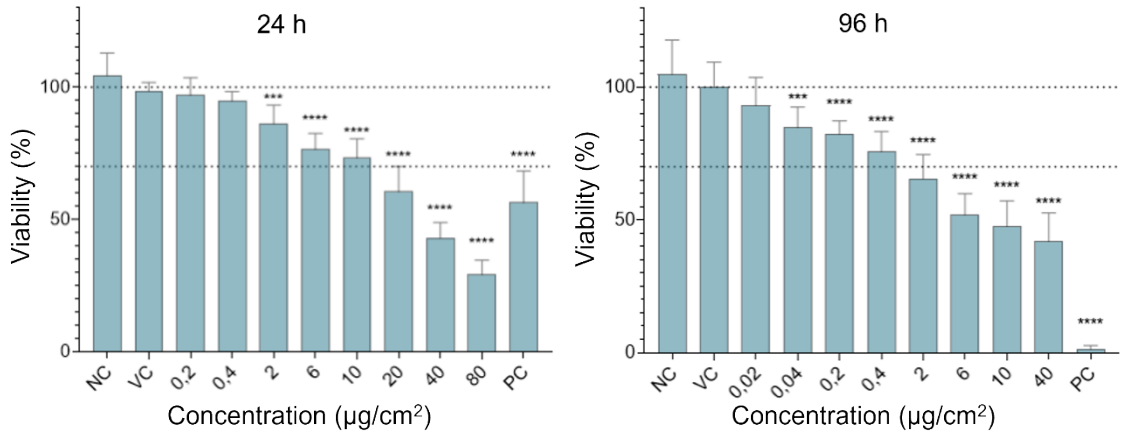

*Figure 6. Cytotoxicity of glucose-coated FeO@Fe_3O_4 MNPs for HepG2 spheroids. Cell viability was measured by using the CellTiter-Glo assay. The panels show cell viability after 24- and 96-hour exposure to graded concentrations of the nanoparticles (0.2 to 80 µg/cm² and 0.02 to 40 µg/cm², respectively). Data is presented relative to the vehicle control (VC; up to 3% Milli-Q water in cell media). NC – cell culture media, PC - 15% DMSO. **** denotes statistically significant difference between the vehicle control and MNPs exposed cells, ANOVA; Dunnett's Multiple Comparison test, ***P < 0.001, ****P < 0.0001).*

The surfaces of iron oxide nanoparticles are known to be capable of catalytically generating reactive oxygen species (ROS) through the Fenton and Haber-Weiss reactions,[35] consequently leading to oxidative stress.[36] Physico-chemical characterization of FeO@Fe_3O_4 MNPs showed that the tested nanoparticles are capable of free radical generation, which may react with different cellular macromolecules, such as DNA, cell membranes or proteins, eventually leading to different pathological and toxicological processes.[37] In our study, malondialdehyde (MDA) was measured as a marker of lipid peroxidation, since it is one of the most frequently used biomarkers of oxidative stress.[38] The results (Figure 7) showed no significant increase in MDA formation in a concentration range up to 20 µg/cm² at 4 or 24 hours of exposure. Tested concentrations were determined based on the results of the cell viability assay in a way that the highest tested concentration did not decrease cell viability by more than 25-30 %.

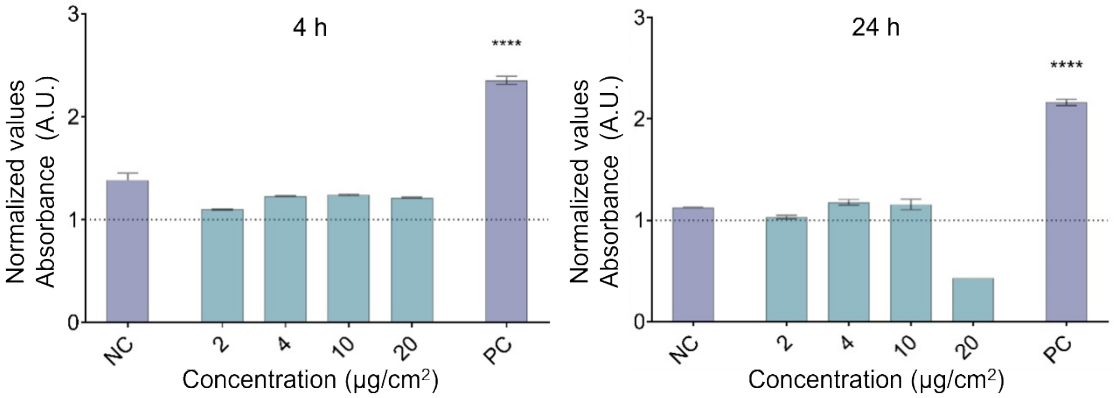

*Figure 7. MDA formation after exposure to glucose-coated FeO@Fe_3O_4 MNPs in HepG2 spheroids. MDA was measured by the Lipid Peroxidation (MDA) Assay Kit. The panels show MDA levels after a 4- and 24-hour exposure to graded concentrations of the nanoparticles (from 2 to 20 μg/cm^2). The results are expressed as the normalized values to vehicle control (VC; up to 3% Milli-Q water in cell media), marked as a dotted line. NC is the negative control (media), and PC is the positive control (1 mM tert-Butyl hydroperoxide; tBOOH, 4 h). A statistically significant difference (ANOVA and Dunnett's post-test) between MNPs-exposed cells and the VC is indicated by ****P < 0.0001.*

Potential DNA damage at the level of individual cells was evaluated using single-cell gel electrophoresis (SCGE), commonly known as the comet assay. This assay is capable of detecting various forms of DNA damage, including single- and double-strand breaks (SSBs and DSBs), alkali-labile sites such as apurinic/apyrimidinic (AP) sites, DNA-DNA and DNA-protein cross-links, oxidized and alkylated bases, UV-induced cyclobutane pyrimidine dimers, and certain chemically induced DNA adducts.[39,40] Furthermore, it can detect transient SSBs that appear during DNA damage repair.[41] Exposure of HepG2 spheroids to graded concentrations of FeO@Fe_3O_4 MNPs (up to 10 μg/cm^2) resulted in no significant increase in DNA damage, as shown in Figure 8.

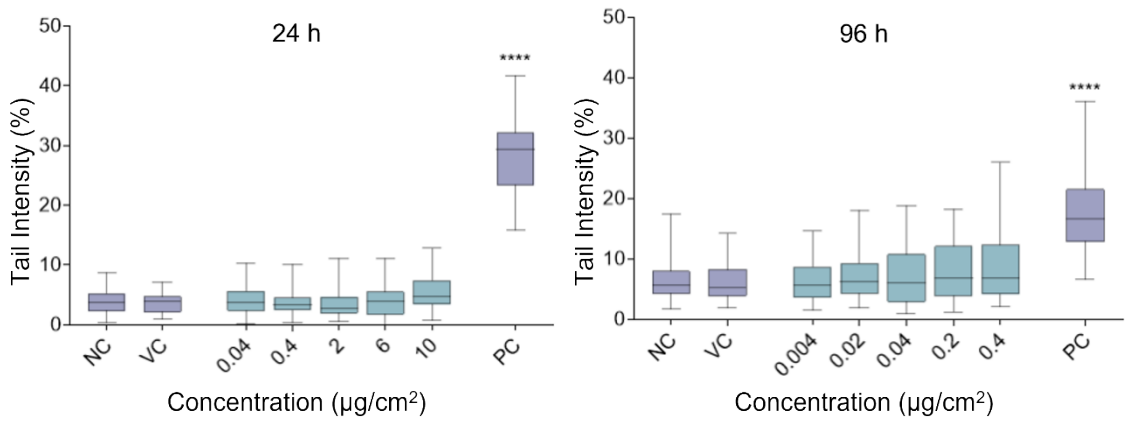

*Figure 8. Potential DNA damage induction by glucose-coated FeO@Fe_3O_4 MNPs in HepG2 spheroids. DNA damage was assessed by using the comet assay, measuring the percentage of DNA in the comet tail. The panels show results after 24- and 96-hour exposure to graded concentrations of the nanoparticles (0.04 to 10 µg/cm² and 0.004 to 0.4 µg/cm², respectively). Data are presented as quantile box plots. The edges of the box represent the 25th and 75th percentiles, the median is a solid line through the box, and the error bars represent 95% confidence intervals. PC is the positive control (30 µM and 5 µM BaP for 24 and 96 h, respectively). A statistically significant difference (Kruskal-Wallis and Dunn's post-test) between MNPs-exposed cells and the vehicle control (VC; up to 3% Milli-Q water in cell media) is indicated by ****P < 0.0001.*

To verify that the tested FeO@Fe_3O_4 MNPs do not induce DNA DSB or exhibit aneugenic activity, further evaluation was performed using immunofluorescent labelling of the DSB biomarker gH2AX and the aneugenicity marker phospho-histone H3 (p-H3), followed by flow cytometric analysis.

DNA DSBs trigger the rapid phosphorylation of histone H2AX, a component of the nucleosomal histone octamer. The phosphorylated form, gH2AX, accumulates at DSB sites, forming nuclear foci that correlates directly with the extent of DNA damage. This makes gH2AX a well-established biomarker for DSB induction and clastogenic activity.[42] Similarly, histone H3 becomes phosphorylated during mitosis to facilitate chromosome condensation and segregation. Since aneugenic compounds can induce this phosphorylation, p-H3 serves as a reliable biomarker for mitotic activity and aneugenic effects.[43]

Analysis of the induction of DNA DSBs and p-H3-positive events after exposure to the tested FeO@Fe_3O_4 MNPs confirmed that none of them induced the formation of DSBs (Figure 9A), nor increased the percentage of p-H3-positive events (Figure 9B), at any of the concentrations tested.

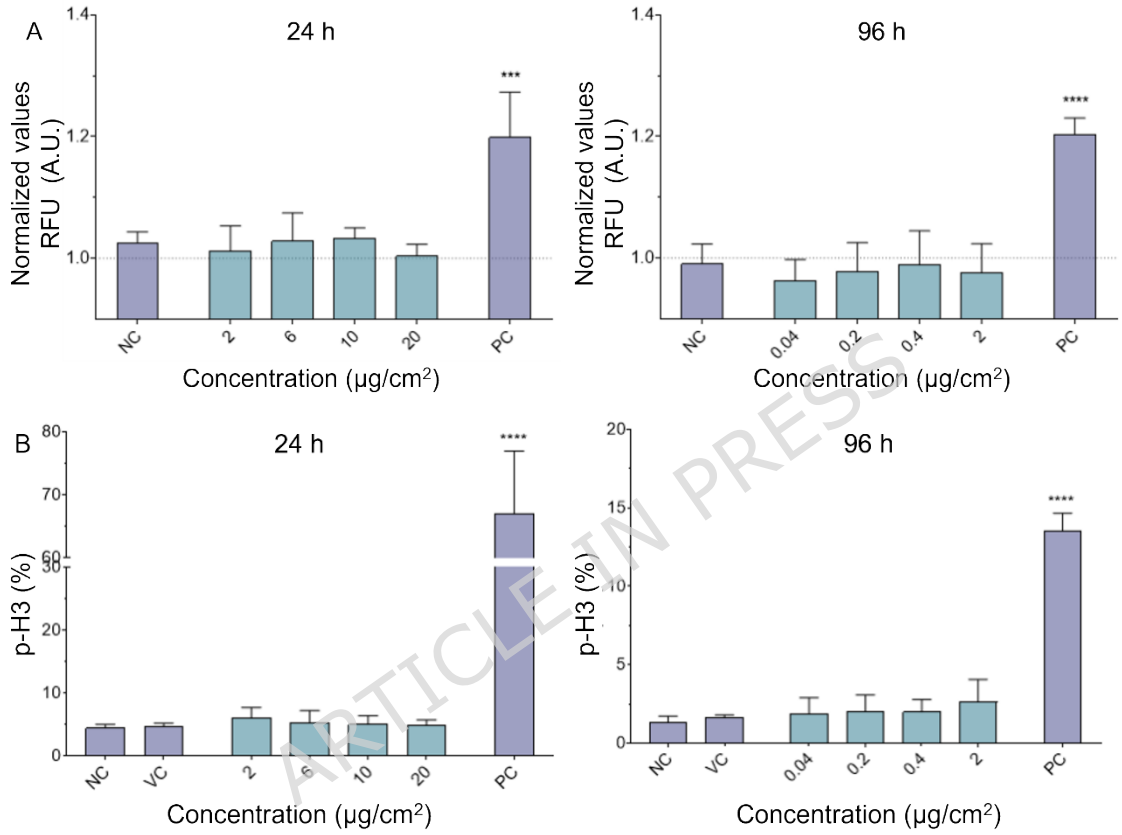

*Figure 9. Potential induction of DNA double-strand breaks (DSBs) and p-H3 positive events by glucose-coated FeO@Fe_3O_4 MNPs in HepG2 spheroids. A) The fluorescence intensity of γH2AX was measured in individual cells by flow cytometry and normalized to the vehicle control (VC; up to 3% Milli-Q water in cell culture media), represented by dotted line. Cells were exposed to increasing concentrations of the nanoparticles for 24 hours (up to 20 µg/cm²) and 96 hours (up to 2 µg/cm²). Etoposide (1.7 µM) served as a positive control (PC). Statistically significant differences between MNPs–treated cells and the VC were determined using ANOVA, followed by Dunnett's post-test and are indicated as ****P < 0.0001. B) The average percentage of p-H3–positive events, indicative of mitotic activity, was also determined by flow cytometry following exposure to graded concentrations of the nanoparticles for 24 hours (up to 20 µg/cm²) and 96 hours (up to 2 µg/cm²). Colchicine (0.1 µM) was used as a positive control. Significant differences compared to the VC (up to 3% Milli-Q water in cell media) were identified by ANOVA and Dunnett's post-test and are marked as ****P < 0.0001.*

The above description shows that the limited penetration depth observed for the FeO@Fe_3O_4 MNPs could be connected to the low genotoxicity observed.[44] Namely, the average spheroid diameter of ~320 µm (Figure S8) implies a

medium spheroid volume of ~1.7×10^7 μm^3. A very approximate estimation yields a number of ~2.6×10^4 cells/spheroid. The penetration depth observed from TEM of 7-10 mm implies that the volume of the rim accessible to nanoparticles is ≈7-9×10^5 mm^3, i.e., ≈3-5×10^3 cells in the rim, which represents 12-17 %of the total spheroid volume. Thus, the majority of cells within the spheroid remain physically separated from the nanoparticles and are not directly exposed to them. It is known that, once nanoparticles are internalized through endocytic pathways, they can be transported through the endolysosomal network within membrane-bound vesicles by motor proteins and cytoskeletal elements.[45] This vesicular sequestration likely acts as a protective mechanism for the cell's core structures, limiting the nanoparticles' access to sensitive targets such as nuclear DNA. To reach cytoplasmic or nuclear components, nanoparticles must first escape the endolysosomal compartment; only then can they directly interact with genomic DNA.[46,47]

On the other hand, despite the low penetration observed, FeO@Fe_3O_4 MNPs exhibited dose- and time-dependent cytotoxicity. In general, several mechanisms may underline the cytotoxicity induced by iron-based nanoparticles. Extracellularly, iron-based nanoparticles can generate ROS that mechanically disrupt the plasma membrane by creating nanoscale pores, or bind to membrane proteins such as NADPH oxidase, Ca^{2+} channels, and various receptors. These interactions can trigger oxidative signaling pathways, elevate intracellular Ca^{2+} levels, and activate downstream second-messenger cascades. Additional intracellular mechanisms may include ROS generation

following internalization of those nanoparticles, lysosomal destabilization, disruption of the cytoskeleton through direct interactions with structural proteins, and the induction of protein conformational changes.[48] Nevertheless, once internalized, nanoparticles may interfere with mitochondrial metabolism, leading to impaired ATP production and activation of apoptotic pathways.[49–51] Since internalization of tested nanoparticles was limited in the present study, cytotoxicity may instead arise from the release of ions from these nanoparticles,[52] especially since no increase in MDA levels and no DNA damage was detected. Namely, ions released from MNPs and consequently iron overload could interfere with mitochondrial iron homeostasis[53] and electron transport, impairing energy metabolism and leading to metabolic failure before the onset of widespread lipid peroxidation.[54,55] Such mitochondrial impairment may represent an early event in iron-dependent cell death pathways, such as ferroptosis, which can be initiated by iron dysregulation and localized redox imbalance before detectable changes in oxidative stress markers, such as MDA.[56]

While a complete determination of the exact mechanisms underlying the observed cytotoxicity is beyond the scope of this work, we would like to emphasize that, although certain aspects of nanoparticle toxicity can be reasonably predicted using *in vitro* assays, it remains challenging to determine whether the detected cytotoxic responses are truly indicative of clinically relevant effects. The absence of genotoxic activity observed in our system is a fundamental step since genotoxicity poses a major barrier to clinical

translation. Still, the dose- and time-dependent cytotoxicity observed highlights the need to carefully assess exposure limits and underscores the importance of balancing therapeutic benefit with potential off-target effects.

Moreover, the absence of detectable genotoxicity, despite the radical-generating capacity demonstrated by EPR, can be discussed in light of the observed TEM localization patterns. In the analyzed sections, MNPs were predominantly found at the spheroid periphery and frequently within membrane-bound vesicles, which may reduce direct access to nuclear DNA. Sparse cytosolic events were also observed, but the present data do not allow inference about their downstream intracellular consequences. Accordingly, the TEM observations provide a plausible qualitative explanation for the lack of genotoxicity, although they cannot be considered conclusive regarding the intracellular origin of the ATP decline or on localized oxidative processes within specific compartments.

Conclusions

The present work showed that FeO@Fe_3O_4 core–shell MNPs with a glucose coating displayed sustained redox activity, while their hydrophilic coating nature enabled penetration through intercellular spaces and cellular uptake. A tightly coupled biphasic lattice (27% FeO / 73% Fe_3O_4) architecture selectively catalyzed hydroperoxyl formation (>50 pM •OOH in 10 min) under near-physiological conditions, outpacing hydroxyl production. These MNPs produced a dose- and time-dependent cytotoxicity (IC_{50} ≈10.8 μg/cm², 96 h)

without significant lipid peroxidation in HepG2 spheroids. Cross-sectional spheroid images analyzed by TEM showed that MNPs were able to penetrate to ≈10–15 mm, therefore delineating an essentially one-cell-thick peripheral rim where most MNPs accumulated, with only sparse particles deeper in the tissue (up to ~30 mm from the spheroid surface). This internalization behavior provides a plausible explanation for the absence of genotoxicity by protecting the cell's core structures from direct damage. The lack of lipid peroxidation indicates no severe oxidative stress after exposure to the MNPs. This suggests that the cytotoxicity, observed as an ATP decline, originated from a different mechanism. Although the present data do not establish the underlying intracellular pathway, they are compatible with mitochondrial dysfunction. Our results suggest a clear structure–activity relationship: the redox-active Fe^{2+} in $FeO@Fe_3O_4$ modulates Fenton-like catalysis, and the glucose coating governs colloidal stability, cellular uptake and spheroid penetration. These findings represent a safe operational window in which $FeO@Fe_3O_4$ nano-reactors can deliver controlled oxidative effects without off-target genotoxicity, supporting their further development as remotely activatable catalysts for oxidative nanomedicine and other biologically integrated redox applications.

Acknowledgements

M.A.M.O. thanks Dr. D. Zákutná and MultiFUN group for their hospitality and supervision at Charles University, and Dr. Milan Dopita from Math and Physics Faculty for facilitating SAXS data acquisition. We are grateful to M. Soriano for

helpful discussions and for the preparation of biological samples for TEM analysis.

Funding

This research was funded by H2020-MSCA NESTOR project (101007629), the HE CutCancer project (101079113), ARIS P1-0245, ARIS J1-4395, ARIS MR grant to IR. E.L. and E.L.W: acknowledge financial support from PICT-2019-02059.

Conflicts of interest

The authors declare there are no conflicts of interest.

Data availability

The datasets generated and analyzed during the current study are available in the Zenodo repository, https://zenodo.org/records/18205062. Additional data (or any materials not included in the repository) are available from the corresponding author upon reasonable request.

References

1. Santos, L. F. *et al.* Remote-Controlled Magnetic Stimulation of Cell-Based Bioengineered Tissues for In Situ Bone Regeneration. *Advanced Materials* **37**, 2500657 (2025).

2. Falconieri, A. *et al.* Magnetically-actuated microposts stimulate axon growth. *Biophys. J.* **121**, 374–382 (2022).

3. De Jong, W. H. & Borm, P. J. *Drug Delivery and Nanoparticles: Applications and Hazards*. *International Journal of Nanomedicine* vol. 3 https://www.dovepress.com/ (2008).

4. Han, X., Xu, K., Taratula, O. & Farsad, K. Applications of nanoparticles in biomedical imaging. *Nanoscale* vol. 11 799–819 Preprint at https://doi.org/10.1039/c8nr07769j (2019).

5. Chen, J. *et al.* Immuno gold nanocages with tailored optical properties for targeted photothermal destruction of cancer cells. *Nano Lett.* **7**, 1318–1322 (2007).

6. Zheng, C. *et al.* Redox-Activatable Magnetic Nanoarchitectonics for Self-Enhanced Tumor Imaging and Synergistic Photothermal-Chemodynamic Therapy. *Small Methods* **8**, 2301099 (2024).

7. Huo, M., Wang, L., Wang, Y., Chen, Y. & Shi, J. Nanocatalytic Tumor Therapy by Single-Atom Catalysts. *ACS Nano* **13**, 2643–2653 (2019).

8. Iroegbu, A. O. C., Teffo, M. L. & Sadiku, E. R. Cancer therapy with engineered nanozymes: from molecular design to tumour-responsive catalysis. *Nanomedicine* **20**, 1799–1817 (2025).

9. Havelikar, U. *et al.* Comprehensive insights into mechanism of nanotoxicity, assessment methods and regulatory challenges of nanomedicines. *Discover Nano 2024 19:1* **19**, 165- (2024).

10. Gao, L. *et al.* Intrinsic peroxidase-like activity of ferromagnetic nanoparticles. *Nature Nanotechnology 2007 2:9* **2**, 577–583 (2007).

11. Zheng, J. J. *et al.* Optimizing the standardized assays for determining the catalytic activity and kinetics of peroxidase-like nanozymes. *Nature Protocols 2024 19:12* **19**, 3470–3488 (2024).

12. Bowen, H. K., Adler, D. & Auker, B. H. *Electrical and Optical Properties of FeO**. *JOURNAL OF SOLID STATE CHEMISTRY* vol. 12 (1975).

13. Calhount, B. A. *Magnetic and Electric Properties of Magnetite at Low Temperatures**. vol. 94 (1954).

14. Shokrollahi, H. A review of the magnetic properties, synthesis methods and applications of maghemite. *Journal of Magnetism and Magnetic Materials* vol. 426 74–81 Preprint at https://doi.org/10.1016/j.jmmm.2016.11.033 (2017).

15. Sieg, H. *et al.* Particulate iron oxide food colorants (E 172) during artificial digestion and their uptake and impact on intestinal cells. *Toxicology in Vitro* **96**, 105772 (2024).

16. Pereira, M. C., Oliveira, L. C. A. & Murad, E. Iron oxide catalysts: Fenton and Fentonlike reactions – a review. *Clay Miner.* **47**, 285–302 (2012).

17. Štampar, M., Tomc, J., Filipič, M. & Žegura, B. Development of in vitro 3D cell model from hepatocellular carcinoma (HepG2) cell line and its application for genotoxicity testing. *Arch. Toxicol.* **93**, 3321–3333 (2019).

18. *Study Report and Preliminary Guidance on the Adaptation of the In Vitro Micronucleus Assay (OECD TG 487) for Testing of Manufactured Nanomaterials*. (2022).

19. Francisco, S. & Francisco, S. γ-H2AX – A Novel Biomarker for DNA Double-strand Breaks. *In Vivo (Brooklyn).* **22**, (2008).

20. Recoules, C., Huertas, C., Vignard, J. & Audebert, M. Comparison of different techniques for γH2AX/pH3 biomarkers quantification for chemical genotoxicity assessment. *Mutat. Res. Genet. Toxicol. Environ. Mutagen.* **906**, 503878 (2025).

21. Fleet, M. E. The Structure of Magnetite. *Structural Science* **37**, 917–920 (1981).

22. Jette, E. R. & Foote, F. An x-ray study of the wüstite (FeO) solid solutions. *J. Chem. Phys.* **1**, 29–36 (1933).

23. Fjellvå, H., Grønvold, F., Stølen, S. & Hauback, B. *On the Crystallographic and Magnetic Structures of Nearly Stoichiometric Iron Monoxide*. *JOURNAL OF SOLID STATE CHEMISTRY* vol. 124 (1996).

24. Testa-Anta, M., Rodríguez-González, B. & Salgueiriño, V. Partial FeO–Fe3O4 Phase Transition Along the <111> Direction of the Cubic Crystalline Structure in Iron Oxide Nanocrystals. *Particle and Particle Systems Characterization* **36**, (2019).

25. Arndt, B. *et al.* Atomic structure and stability of magnetite Fe3O4(001): An X-ray view. *Surf. Sci.* **653**, (2016).

26. Aadinath, W. & Muthuvijayan, V. Influence of oleic acid coating on the magnetic susceptibility and Fenton reaction-mediated ROS generation by the iron oxide nanoparticles. *Nano Express* **5**, (2024).

27. Ibrahim, M., Alaam, M., El-Haes, H., Jalbout, A. F. & De Leon, A. Analysis of the structure and vibrational spectra of glucose and fructose. *Ecletica Quimica* **31**, (2006).

28. Petcharoen, K. & Sirivat, A. Synthesis and characterization of magnetite nanoparticles via the chemical co-precipitation method. *Materials Science and Engineering: B* **177**, 421–427 (2012).

29. Gutteridge, J. M. Reactivity of hydroxyl and hydroxyl-like radicals discriminated by release of thiobarbituric acid-reactive material from deoxy sugars, nucleosides and benzoate. *Biochem. J.* **224**, (1984).

30. Bothe, E., Schulte-Frohlinde, D. & Von Sonntag, C. Radiation chemistry of carbohydrates. Part 16.† Kinetics of HO 2 elimination from peroxyl radicals derived from glucose and polyhydric alcohols. *Journal of the Chemical Society, Perkin Transactions 2* https://doi.org/10.1039/p29780000416 (1978) doi:10.1039/p29780000416.

31. Park, J. S. B., Wood, P. M., Davies, M. J., Gilbert, B. C. & Whitwood, A. C. A kinetic and ESR investigation of Iron(II) oxalate oxidation by hydrogen peroxide and dioxygen as a source of hydroxyl radicals. *Free Radic. Res.* **27**, (1997).

32. Bashiri, G. *et al.* Nanoparticle protein corona: from structure and function to therapeutic targeting. *Lab on a Chip* vol. 23 1432–1466 Preprint at https://doi.org/10.1039/d2lc00799a (2023).

33. Štampar, M., Breznik, B., Filipič, M. & Žegura, B. Characterization of In Vitro 3D Cell Model Developed from Human Hepatocellular Carcinoma (HepG2) Cell Line. *Cells* **9**, (2020).

34. Waldherr, M. *et al.* Use of HuH6 and other human-derived hepatoma lines for the detection of genotoxins: a new hope for laboratory animals? *Arch. Toxicol.* **92**, 921–934 (2018).

35. Wydra, R. J., Oliver, C. E., Anderson, K. W., Dziubla, T. D. & Hilt, J. Z. Accelerated generation of free radicals by iron oxide nanoparticles in the presence of an alternating magnetic field. *RSC Adv.* **5**, 18888–18893 (2015).

36. Pizzino, G. *et al.* Oxidative Stress: Harms and Benefits for Human Health. *Oxid. Med. Cell. Longev.* **2017**, 8416763 (2017).

37. De Zwart, L. L., Meerman, J. H. N., Commandeur, J. N. M. & Vermeulen, N. P. E. Biomarkers of free radical damage: Applications in experimental animals and in humans. *Free Radic. Biol. Med.* **26**, 202–226 (1999).

38. Khoubnasabjafari, M., Ansarin, K. & Jouyban, A. Reliability of malondialdehyde as a biomarker of oxidative stress in psychological disorders. *Bioimpacts* **5**, 123–127 (2015).

39. Møller, P. *et al.* Minimum Information for Reporting on the Comet Assay (MIRCA): recommendations for describing comet assay procedures and results. *Nature Protocols 2020 15:12* **15**, 3817–3826 (2020).

40. Collins, A. *et al.* Measuring DNA modifications with the comet assay: a compendium of protocols. *Nat. Protoc.* **18**, 929–989 (2023).

41. Collins, A. R. The comet assay for DNA damage and repair: principles, applications, and limitations. *Mol. Biotechnol.* **26**, 249–261 (2004).

42. Bonner, W. M. *et al.* γH2AX and cancer. *Nature Reviews Cancer* vol. 8 Preprint at https://doi.org/10.1038/nrc2523 (2008).

43. Prigent, C. & Dimitrov, S. Phosphorylation of serine 10 in histone H3, what for? *J. Cell Sci.* **116**, (2003).

44. Chen, W. *et al.* Size-Dependent Penetration of Nanoparticles in Tumor Spheroids: A Multidimensional and Quantitative Study of Transcellular and Paracellular Pathways. *Small* **20**, (2024).

45. Shang, L., Nienhaus, K. & Nienhaus, G. U. *Engineered Nanoparticles Interacting with Cells: Size Matters*. http://www.jnanobiotechnology.com/content/12/1/5 (2014) doi:10.1186/1477-3155-12-5.

46. Maria, M. F. *et al.* Evaluating Nanoparticle-Induced Cytotoxicity: Mechanisms and Methods. *Nano Biomedicine and Engineering* vol. 17 Preprint at https://doi.org/10.26599/NBE.2025.9290129 (2025).

47. Shukla, R. K., Badiye, A., Vajpayee, K. & Kapoor, N. Genotoxic Potential of Nanoparticles: Structural and Functional Modifications in DNA. https://doi.org/10.3389/fgene.2021.728250 doi:10.3389/fgene.2021.728250.

48. nanomedicine, E. F.-I. journal of & 2012, undefined. The role of surface charge in cellular uptake and cytotoxicity of medical nanoparticles. *Taylor & FrancisE FröhlichInternational journal of nanomedicine, 2012•Taylor & Francis* **7**, 5577–5591 (2012).

49. Napolitano, G., Fasciolo, G. & Venditti, P. Mitochondrial management of reactive oxygen species. *Antioxidants* vol. 10 Preprint at https://doi.org/10.3390/antiox10111824 (2021).

50. Zhang, B. *et al.* Role of mitochondrial reactive oxygen species in homeostasis regulation. *Redox Report* vol. 27 Preprint at https://doi.org/10.1080/13510002.2022.2046423 (2022).

51. Rivas-García, L. *et al.* Ultra-small iron nanoparticles target mitochondria inducing autophagy, acting on mitochondrial dna and reducing respiration. *Pharmaceutics* **13**, (2021).

52. Dzeranov, A. *et al.* Iron Oxides Nanoparticles as Components of Ferroptosis-Inducing Systems: Screening of Potential Candidates. *Magnetochemistry* **9**, (2023).

53. Dietz, J. V., Fox, J. L. & Khalimonchuk, O. Down the iron path: Mitochondrial iron homeostasis and beyond. *Cells* vol. 10 Preprint at https://doi.org/10.3390/cells10092198 (2021).

54. Zhang, T. guang, Zhang, Y. long, Zhou, Q. qian, Wang, X. hui & Zhan, L. sheng. Impairment of mitochondrial dynamics involved in iron oxide nanoparticle-induced dysfunction of dendritic cells was alleviated by autophagy inhibitor 3-methyladenine. *Journal of Applied Toxicology* **40**, (2020).

55. Zhao, Y., Yang, M. & Liang, X. The role of mitochondria in iron overload-induced damage. *J. Transl. Med.* **22**, (2024).

56. Zhang, S. *et al.* Double-edge sword roles of iron in driving energy production versus instigating ferroptosis. *Cell Death and Disease* vol. 13 Preprint at https://doi.org/10.1038/s41419-021-04490-1 (2022).

Glucose coated $FeO@Fe_3O_4$ nanoparticles show tunable catalytic reactivity and safety in a 3D hepatic *in vitro* model.

Marco A. Morales Ovalle[a,b,c,d,e#], Iza Rozman[f,g#], Elin L. Winkler[a,b,c], Enio Lima Jr.[a,b], Alja Štern[f,g], Katja Kološa[f], Bojana Žegura[f,g], and Gerardo F. Goya[d,e*]

[a] *Departamento de Magnetismo y Materiales Magnéticos, Gerencia de Física, Centro Atómico Bariloche, S. C. de Bariloche, 8400, Argentina*

[b] *Instituto de Nanociencia y Nanotecnología, CNEA/CONICET, Centro Atómico Bariloche, S. C. Bariloche, 8400, Argentina*

[c] *Instituto Balseiro, UNCuyo/CNEA, Centro Atómico Bariloche, S. C. Bariloche, 8400, Argentina*

[d] *Departamento de Fisica de la Materia Condensada, Universidad de Zaragoza, Zaragoza, Spain*

[e] *Instituto de Nanociencia y Materiales de Aragón, CSIC-Universidad de Zaragoza, Zaragoza, Spain*

[f] *National Institute of Biology, Department of Genetic Toxicology and Cancer Biology, Ljubljana, Slovenia.*

[g] *Biotechnical Faculty, University of Ljubljana, Slovenia*

*Correspondence: goya@unizar.es

[#] These authors contributed equally to this work.

Abstract

Iron-oxide magnetic nanoparticles (MNPs) have been extensively investigated as magnetically actable nanocatalysts for diagnostic and therapeutic applications. However, because wüstite/magnetite/maghemite phases can interconvert, coexisting Fe^{2+}/Fe^{3+} species may redirect Fenton-like chemistry and generate reactive oxygen species (ROS) profiles that differ from the intended biocatalytic pathway. Here we investigate monodisperse biphasic $FeO@Fe_3O_4$ core-shell MNPs with average particle size ⟨d⟩ = 9.6(5) nm, and their glucose-coated analogue, combining EPR radical analysis with toxicity testing in a 3D HepG2 hepatic spheroid model. Naked particles exhibited conventional Fenton-like behavior dominated by hydroxyl radicals (•OH), whereas glucose coating markedly suppressed •OH while increasing hydroperoxyl radicals (•OOH; ≈55 pM at 60 min), demonstrating ligand-controlled rerouting of the radical pathway. TEM mapping across spheroid cross-sections showed preferential MNP accumulation in the outer layer, with most observed events confined to the outer □10-15 mm, corresponding to an approximately one-cell-thick rim; sparse deeper events were observed up to □30-35 mm. MNPs produced dose- and time-dependent cytotoxicity in HepG2 spheroids, with IC_{50} values of 29.3 (24 h) and 10.8 (96 h) $mg \cdot cm^{-2}$, without evidence of lipid peroxidation or genotoxicity. MDA levels remained unchanged, the comet assay showed no increase in DNA damage, and gH2AX and phospho-H3 (p-H3) positive events were not detected. Our results show that glucose functionalization provides a simple route to modulate radical

pathways and define operational windows for redox-active FeO@Fe_3O_4 nano-reactors in oxidative nanomedicine.

Keywords: iron-oxide nanoparticles, Fenton-like catalysis, cytotoxicity, genotoxicity, HepG2 spheroids

Introduction

An increasing number of targeted therapies with innovative strategies for cancer treatments are based on the ability of magnetic nanoparticles (MNPs) to be remotely actuated by magnetic fields.[1,2] This physical property and their tunable surface chemistry make them particularly suitable for biomedical applications.[3–5] Thus, oncology strategies are seeking for such systems, adequately optimized, that could exploit both an efficient magnetic actuation and a controllable redox reactivity at the tumor interface.[6] Previous reports on MNPs capable of maintaining the Fe^{2+}/Fe^{3+} cycle to catalyze peroxide activation Fenton-like pathways in acidic, H_2O_2-enriched microenvironments characteristic of many solid tumors have already shown partial success.[7] Despite their promise for biotechnological applications, it is increasingly evident that current MNPs remain suboptimal in atomic-level design control,[8] and that a more rigorous understanding of their interactions with biological systems (together with comprehensive safety evaluation) is still required.[9]

Conversely, in other bio-based applications, the very same generation of reactive oxygen species (ROS) by certain iron-oxide phases is problematic, since oxidative stress and enzyme-like reactivity can introduce off-target biological effects and compromise the intended functionality.[10,11] The diverse surface reactivities of several iron oxide phases commonly used in biomedical

applications, such as magnetite Fe_3O_4 and maghemite g-Fe_2O_3 (and, less frequently, wüstite FeO) makes it difficult to predict their type of behavior in biological media.[12–15] These oxides can show a different catalytic role in Fenton-like reactions and, consequently, in their ROS generation capacity and biological impact.[16] Understanding how specific iron oxide phases and their combinations affect these properties is essential for defining their potential toxicity.

In this study, we engineered glucose-coated FeO@Fe_3O_4 core-shell nanoparticles aiming at a system with a coupled electron-rich (wüstite) core with a magnetite shell, creating a biphasic architecture that simultaneously enhances magnetic responsiveness and surface redox activity. By integrating thorough physicochemical insight with evaluation of their potential (geno)toxic effects in a three-dimensional (3D) human hepatic cell model prepared from the HepG2 cell line, we establish direct links between nanoscale structure, controlled •OOH radical generation, and their biological effects *in vitro*. Our findings position biphasic magnetic nanoparticles as tunable, remotely activatable oxidative nano-effectors for precision therapeutic applications.

Materials and Methods

Reagents

Iron(III) acetylacetonate ($Fe(acac)_3$, 97%), oleic acid (analytical standard), and trioctylamine (98%) were used for nanoparticle synthesis. Toluene (≥99.5%) and acetone (≥99.5%) were used for washing and dispersion. Anhydrous glucose (99.8%) and ammonium hydroxide solution (27% w/w) were employed

for the coating step. Unless otherwise stated, chemicals were purchased from Sigma-Aldrich (Merck) and used as received without further purification. Dulbecco's phosphate-buffered saline (DPBS) 10× (Gibco) was diluted to 1× with sterile water and used for washing coated nanoparticles; sterile water was also used for the final resuspension. For spin-trapping assays, EPR-grade 5,5-dimethyl-1-pyrroline N-oxide (DMPO, ≥97%; Sigma-Aldrich) served as the spin trap. Ultrapure water (Milli-Q, 18.2 MΩ·cm) and a 10 mM acetate buffer adjusted to pH 5 were used as dispersion media in these experiments. MEM medium (MEM-10370-046) and Fetal Bovine Serum (FBS, 10%) for cell culture and spheroid preparation were obtained from Gibco (Paisley, Scotland, UK). Sodium pyruvate (1 mM), L-glutamine (2 mM), penicillin/streptomycin (100 IU/mL), Non-Essential Amino Acids (NEAA) and methylcellulose were purchased from Sigma-Aldrich (St. Louis, MO, USA). The CellTiter-Glo® Luminescent Cell Viability Assay for the cytotoxicity evaluation was acquired from Promega (Madison, WI, USA) to quantify ATP levels. Dimethyl sulfoxide (DMSO) was obtained from Sigma Aldrich (Missouri, U. S.) and used as a positive control. The Lipid Peroxidation (MDA) Assay Kit for the MDA assay was obtained from Abcam (Cambridge, UK) to measure lipid peroxidation. tert-Butyl hydroperoxide (tBOOH) was purchased from Micropolo (Maribor, Slovenia) and used as a positive control. For the preparation of single cell suspensions, Collagenase was obtained from Thermo Fisher Scientific (Waltham, Massachusetts, U.S.). GelRed nucleic acid stain was acquired from Biotium (USA) and used for slide analysis. Benzo[a]pyrene purchased from

Merck (New Jersey, U. S.), etoposide and colchicine (both purchased from Sigma, St. Louis, MO, USA) served as positive controls. Paraformaldehyde (PFA, 4%) for flow cytometry analysis was obtained from Merck (New Jersey, U. S.) and used for cell fixation. Bovine Serum Albumin (BSA, 1%) was obtained from Sigma (St. Louis, Missouri, U. S.) and used for antibody incubation. The following antibodies were acquired from Miltenyi Biotech (Germany): γH2AX pSer139-APC (130-123-256) and pH3-PE (130-105-700). REA controls (Miltenyi Biotech) were included for non-specific antibody binding assessment. Etoposide (1.7 µM) and colchicine (0.1 µM), purchased from ChemCruz (Dallas, U. S.) and Merck (New Jersey, U. S.), respectively, were used as positive controls.

Nanoparticle Synthesis

$FeO@Fe_3O_4$ nanoparticles were obtained by thermal decomposition of organometallic precursors in trioctylamine. Iron(III) acetylacetonate (1 mmol) and oleic acid (3 mmol) were dispersed in trioctylamine (15 mL) in a three-neck round-bottom flask under mechanical stirring. The mixture was heated under a nitrogen atmosphere (»3.7 $L \cdot min^{-1}$) from room temperature to 200 °C, with a temperature increase of 5 ± 2 $°C \cdot min^{-1}$,and from 200 °C to 350 °C, with a temperature increase of 18 ± 6 $°C \cdot min^{-1}$. A water-cooled Allihn condenser (see Figure S1) was used throughout. Upon reaching 350 °C, the heating mantle was removed, and the reaction was allowed to cool to room temperature. The crude product was a homogeneous black dispersion that was weakly magnetically responsive. To collect the as-prepared material, the

resulting dark solution was treated with toluene and acetone in a 1:1:5 ratio in an Erlenmeyer flask to prevent solvent evaporation. A precipitate was obtained through magnetic decantation. Subsequently, the as-prepared precipitate was subjected to an organic excess removal protocol to obtain the labelled non-coated nanoparticles. The precipitate was repeatedly suspended in toluene, diluted in acetone, and magnetically precipitated; this cycle was performed until no further changes were observed in the FTIR spectra of the supernatant or the solid. It should be noted that while this process significantly reduces the organic layer to allow for aqueous interaction, trace amounts of hydrophobic residues remained on the nanoparticle surface. Samples of pure magnetite Fe_3O_4, used as control, were synthesized through the same route, but using different solvent and temperature profile (see Figures S3 and S4), as described in the Supplementary Material.

Glucose Coating Procedure

For the glucose coating procedure, non-coated $FeO@Fe_3O_4$ nanoparticles were suspended through sonication in a glucose-ammonium hydroxide solution at a 1:10 (w/v) ratio, which was prepared by dissolving anhydrous glucose in a 27% ammonium hydroxide solution (glucose mass being 5 times the initial nanoparticle weight). The mixture was then kept overnight with mechanical agitation. The entire coating process, including subsequent washing steps with PBS, was conducted under sterile conditions. Due to the excellent dispersion of the nanoparticles in water, recovery of the glucose-coated nanoparticles involved diluting the suspension in sterile PBS, centrifuging, and carefully

removing the supernatant while the pellet was held immobilized by a magnet. This washing process was repeated until a neutral pH was reached. Finally, the recovered glucose-coated nanoparticles were resuspended in 1500 µL of sterile water. The concentration of the final solution was determined gravimetrically by drying a known volume of the suspension at 75 °C and weighing the recovered nanoparticles.

Characterization of nanoparticles

Unless otherwise specified, XRD, TEM/SAED/HRTEM, and magnetic characterization were performed on the as-synthesized $FeO@Fe_3O_4$ nanoparticles before glucose coating. FTIR, SAXS, EPR, and all biological experiments were carried out using the glucose-coated material.

Crystallographic Structure

Structural characterization of the nanoparticles was performed using a Bruker D8 Advance powder X-ray diffractometer (Cu Ka, l=0.154 nm) at room temperature. Samples were prepared by depositing a concentrated MNP/acetone suspension onto a rounded glass substrate and allowing the solvent to evaporate completely, forming a tightly adhered dark powder layer.

Nanoparticle Morphology and Size

The morphology and size distribution of the nanoparticles were determined by TEM using a Tecnai T20 (Thermofisher) microscope operated at 200 kV and room temperature. TEM samples were prepared by applying a droplet of a low-concentration (translucent) nanoparticle suspension in toluene onto a carbon-coated copper grid and allowed to dry. A size histogram was obtained from

randomly labelled MNPs (using ImageJ 1.54f software), and the mean diameter and standard deviation were estimated by fitting a log-normal distribution.

Magnetic Properties

The magnetic properties of the nanoparticles were characterized using a S700X Superconducting Quantum Interference Device (SQUID) magnetometer (Quantum Design). Field-dependent magnetization (M vs. H) was measured at 300 K and at 90 K. The exchange bias effect signature was examined after cooling the sample from room temperature to 90 K in the presence of a 10 kOe applied field.

Surface Functionalization

Glucose coating effectiveness was evaluated through ATR-FTIR spectra, recorded at a spectral resolution of 4 cm^{-1} from 500 to 4000 cm^{-1} with a Spectrum Two spectrometer (PerkinElmer). In general, measurements were made by applying a droplet of a concentrated nanoparticle suspension in toluene or Milli-Q water directly onto the ATR crystal, and spectra were recorded as volatile substances evaporated.

Colloidal Properties

Size, polydispersity, and interparticle interactions of the glucose-coated nanoparticles in solution were measured using X-ray scattering at both Cu Kα and Mo Kα wavelengths on a Xenocs Xeuss 2.0 SAXS instrument. The data collected from these two sources were subsequently merged to provide a broader Q-range for analysis. The solution was contained in a 1.5 mm diameter borosilicate glass tube. Scattering Length Densities (SLDs) for the various

components were calculated using the NIST Center for Neutron Research (NCNR) scattering length density calculator, specifically for the Cu Kα source. These calculations were based on the known bulk densities of 5.41 g cm^{-3} for FeO, 5.17 g cm^{-3} for Fe_3O_4, 1.56 g cm^{-3} for glucose, and 1 g cm^{-3} for water. Data analysis and model fitting were performed using SasView 6.0.1 software.

Given the proximity in Scattering Length Densities (SLDs) of the FeO core (44.607×10^{-6} $Å^{-2}$) and Fe_3O_4 shell (40.452×10^{-6} $Å^{-2}$), as well as the low contrast between the glucose coating (14.170×10^{-6} $Å^{-2}$) and the aqueous solvent (9.469×10^{-6} $Å^{-2}$), the nanoparticles were approximated to "homogeneous" spheres with a weighted average SLD of 41.6985×10^{-6} $Å^{-2}$, based on the phase proportions estimated from XRD (ϕ_{core} ~0.3 and ϕ_{shell} ~0.7). All these SLDs were fixed during the whole fitting analysis. A fit to reveal the primary particle contributions was first performed over the Q-range from 5.040×10^{-2} to 4.837×10^{-1} A^{-1}. The distribution of radius from this initial result (0.0794(9)) was then fixed during the subsequent analysis, combining a sphere form factor and a square-well structure factor.

Free Radicals Detection and Quantification

For EPR, the non-coated FeO@Fe_3O_4 reference was evaluated only under acidic conditions (10 mM acetate buffer, pH 5). Water-condition EPR data are reported only for the glucose-coated nanoparticles and the corresponding nanoparticle-free control. The generation of DMPO adducts was determined at room temperature using an ELEXSYS II-E500 EPR spectrometer equipped with an X-band resonant cavity (9.4 GHz). Reaction mixtures for the EPR

experiments were prepared by dispersing 20 mL of glucose-coated $FeO@Fe_3O_4$ MNPs (2 mg/mL) in 20 mL of either a 10 mM pH 5 acetate buffer solution or Milli-Q water (for neutral pH conditions). This was followed by the addition of 10 mL of a DMPO/water solution (0.167 g/mL). The reaction was initiated by the addition of 2 mL of H_2O_2 30% (0.49 M). The solution was contained in a 1 mm diameter Q-band quartz tube. EPR spectra of each solution were recorded simultaneously with an MgO pattern crystal doped with a known concentration of Mn^{2+} attached to the tube, which served as an internal standard for DMPO adduct quantification. All spectra were processed using the Spin Fit software from Bruker. The baseline for each spectrum was computed with a 3rd-degree polynomial and then subtracted. Subsequently, the resonance lines were fitted using the hyperfine parameters of the identified components. The concentrations of DMPO adducts were then determined by comparing the fitted EPR spectrum area of each species with the area of the MgO/Mn^{2+} standard. For EPR, the non-coated $FeO@Fe_3O_4$ reference was evaluated only under acidic conditions (10 mM acetate buffer, pH 5). Water-condition EPR data are reported only for the glucose-coated nanoparticles and the corresponding nanoparticle-free control. In addition, the Fe_3O_4 control experiments (Figure S7 in Supplementary Material) were performed under the same spin-trapping EPR conditions used for $FeO@Fe_3O_4$, including the corresponding non-coated and glucose-coated Fe_3O_4 samples.

Assessment of (geno)toxicity *in vitro*

Cell Cultivation

The *in vitro* model of choice in our study was a 3D cell model (spheroids) derived from the human hepatocellular carcinoma cell line (HepG2) (ATCC HB-8065™, Manassas, VA, USA). Cells were grown in MEM medium supplemented with 10% FBS and 1 mM sodium pyruvate, 2 mM L-glutamine, 100 IU/mL penicillin/streptomycin, and NEAA, at 37 °C in a humidified atmosphere with 5% CO_2.

Spheroid Preparation

The spheroids were prepared using the force floating method as described by Štampar et al. [17]. Cell passages up to 13 were used. In brief, cells were seeded at a density of 3,000 cells per well into 96-well U-bottom plates (Corning Costar Corporation, New York, USA) using complete growth medium supplemented with 4% methylcellulose. The plates were centrifuged at 900 × g for 90 minutes to promote spheroid formation. The resulting spheroids were then incubated for 72 hours at 37 °C in a humidified atmosphere with 5% CO_2 to allow for maturation before experimentation.

Spheroids were exposed to FeO@Fe_3O_4 MNPs at concentrations ranging from 0.01 to 200 µg/mL, corresponding to 0.004 to 80 µg/cm². These concentrations refer to the mass of the whole MNPs. The range was selected based on the OECD Study Report and Preliminary Guidance on the Adaptation of the In Vitro Micronucleus Assay (OECD TG 487) for Testing of Manufactured Nanomaterials (September 2022).[18] Concentrations were calculated per surface area rather

than volume, as the tested $FeO@Fe_3O_4$ MNPs tend to settle onto the surface of the cells when in suspension.

Nanoparticle interaction with the cells in the spheroids – TEM

The study of the MNP's penetration into the 3D architecture of HepG2 spheroids was undertaken through a systematic analysis of sequential transmission electron microscopy (TEM) images along the cross section of the spheroids. After spheroids generated as described above and incubated with a MNPs concentration of 50 μg/mL were harvested, gently rinsed with phosphate-buffered saline (PBS, pH 7.4) to remove non-associated MNPs. The rinsed spheroids were chemically fixed in 2% glutaraldehyde in 0.1 M phosphate buffer (PB, pH 7.2) for 2 h at room temperature, followed by fixation in 1.5% glutaraldehyde in 0.05 M PB at 4 °C overnight. Samples were post-fixed with 1% osmium tetroxide for 1 h at room temperature, dehydrated through a graded ethanol series (30%, 50%, 70%, 90%, and 100%), and infiltrated with epoxy resin. For cross-sectional imaging, resin blocks were polymerized at 60 °C for 48 h, and ultrathin sections (~70 nm) were cut using an ultramicrotome. Sections were collected on copper grids and contrasted with 2% aqueous uranyl acetate and lead citrate. TEM imaging was carried out on a Tecnai T20 microscope (Thermo Fisher Scientific, USA) operating at 200 kV. For each condition at least three spheroids were analyzed. In addition, for one representative spheroid, a continuous linear montage was acquired across the section by collecting consecutive adjacent fields from one outer edge to the opposite border and stitching the images into a single composite.

Oxidative stress induction – MDA Assay

To check the degree of oxidative stress produced by the $FeO@Fe_3O_4$ MNPs, malondialdehyde (MDA) was used as a marker of lipid peroxidation. For this purpose, the Lipid Peroxidation (MDA) Assay Kit (Abcam, Cambridge, UK) was used. This kit measures lipid peroxidation by detecting MDA, which reacts with thiobarbituric acid (TBA) to form a colorimetric/fluorometric product, with intensity proportional to the MDA concentration in the sample. HepG2 spheroids were exposed to graded concentrations of $FeO@Fe_3O_4$ MNPs (2-20 $\mu g/cm^2$) for 4 and 24 hours. Evaluated concentrations were determined based on the results of the cell viability assay in a way that the highest tested concentration did not decrease cell viability by more than 25-30%. At each time point, spheroids were collected, rinsed with 1×PBS, and homogenized in MDA Lysis Buffer supplemented with BHT. The homogenates were centrifuged at 13,000 × g for 10 minutes, and the resulting supernatant was transferred to microcentrifuge tubes containing the TBA solution, prepared according to the manufacturer's instructions. Samples were then incubated at 95 °C for 60 minutes, followed by a 10-minute cooling period in an ice bath. Absorbance at 532 nm was measured using the BioTek Cytation 5 Cell Imaging Multimode Reader (Agilent, Santa Clara, USA). Each experimental condition was tested in triplicate, and the experiment was independently repeated three times. Negative (cell medium), solvent (up to 3% Milli-Q water), and positive (1 mM tBOOH) controls were included in all assays.

Cytotoxicity – measurement of the ATP content

The cytotoxicity of $FeO@Fe_3O_4$ MNPs was assessed using the CellTiter-Glo® Luminescent Cell Viability Assay. This homogeneous method quantifies ATP levels as an indicator of metabolically active, viable cells. HepG2 spheroids were exposed to varying concentrations of $FeO@Fe_3O_4$ MNPs (0.004–80 $\mu g/cm^2$) for 24 and 96 hours. The assay was carried out according to the manufacturer's instructions with slight modifications. Briefly, spheroids in 50 µL of culture medium were transferred to a white opaque 96-well plate, followed by the addition of 50 µL of CellTiter-Glo® reagent per well. The contents were mixed by pipetting to ensure complete cell lysis within the spheroids, and the plate was incubated for 20 minutes at room temperature. Luminescence was then measured using a luminometer (Synergy MX, BioTek, Winooski, VT, USA). Experiments were conducted in five replicates for each condition and repeated independently three times to ensure reproducibility. A negative (cell medium), a solvent (up to 3% Milli-Q water), and a positive control (15% DMSO), were included in the experiments. Significant differences in cell viability between exposed cells and the solvent control group (non-exposed cells) were analyzed using a One-Way Analysis of Variance (ANOVA) and Dunn's multiple comparison test in GraphPad Prism 10 (GraphPad Software, San Diego, CA, USA).

The Alkaline Comet Assay

DNA damage following exposure to $FeO@Fe_3O_4$ MNPs was assessed using the alkaline comet assay. HepG2 spheroids were exposed to graded non-cytotoxic

concentrations of MNPs (0.004–10 μg/cm^2) for 24 and 96 hours. After each exposure period, spheroids were dissociated into single-cell suspensions. Namely, spheroids were collected and washed with 1× PBS, then incubated with a mixture of collagenase , MEM, and TrypLE for 10 min (37 °C, 5% CO_2). Following enzymatic treatment, spheroids were further dissociated by gentle pipetting. Enzymatic activity was subsequently quenched by the addition of complete cell culture medium. The comet assay was performed according to the protocol described by Štampar et al.[17] and the conditions are detailed in Table S3 of the Supplementary Material. Slides were stained with GelRed nucleic acid stain (Biotium, USA) following the manufacturer's instructions, and comet scoring was carried out using a fluorescence microscope and Comet Assay IV software (Instem, Philadelphia, USA). Controls included negative control (cell culture medium), solvent control (up to 3% Milli-Q water), and positive controls (30 μM and 5 μM benzo[a]pyrene for 24 and 96-hour exposures, respectively). Each experiment was independently repeated three times, with 50 nuclei analyzed per experimental point. Statistical analysis was conducted in GraphPad Prism 10 using the Kruskal–Wallis nonparametric test, followed by Dunn's multiple comparison test to evaluate differences in tail DNA percentage between groups.

Analysis of γH2AX and p-H3 positive cells by flow cytometry

To further evaluate the potential genotoxic effects of FeO@Fe_3O_4 MNPs, phosphorylation of two histones – H2AX and H3 – was examined by flow cytometry. Phosphorylated histone H2Ax, forming γH2Ax, is a marker of

double-strand breaks (DSBs),[19] while phosphorylation of H3 (pH3) reflects mitotic cells and is a marker for exposure to aneugenes.[20] Three-day-old HepG2 spheroids were exposed to graded non-cytotoxic concentrations of MNPs (0.04–20 μg/cm^2) for 24 and 96 hours, after which they were dissociated into single-cell suspensions. The cells were washed twice with 1×PBS, fixed in 4% paraformaldehyde (PFA), and stored at 4 °C. Before analysis, cells were washed again with 1×PBS and incubated for 30 minutes in 1% BSA containing antibodies against γH2AX pSer139-APC (130-123-256) and pH3-PE (130-105-700), diluted 1:50. REA controls were included to account for non-specific antibody binding.

Etoposide (1.7 μM) and colchicine (0.1 μM) were used as positive controls, while fixed cells in complete growth medium and medium containing up to 3% Milli-Q water served as negative and solvent controls, respectively. The experiment was repeated three times independently. Samples were analyzed on a MACSQuant Analyzer 10 flow cytometer using MACSQuantify™ (Miltenyi Biotech, Germany) and FlowJo V10 (Becton Dickinson, New Jersey, USA). Statistical analysis was conducted using GraphPad Prism 10.

Results and Discussion

The FeO@Fe_3O_4 MNPs investigated here were intentionally engineered as redox-active, magnetically actable nano-reactors in which controlled ROS fluxes are desirable (e.g., as “oxidative nanomedicine” effectors). The FeO (Fe^{2+}-rich) core coupled to a Fe_3O_4 shell was selected to combine a local reservoir of Fe^{2+}/Fe^{3+} redox pairs that can sustain Fenton-like cycling in the

presence of different substrates. In parallel, the glucose coating was intended to deliberately probe whether a simple, biogenic ligand can tune the radical pathway (shifting the balance away from highly reactive •OH). Because these design choices target eventual biological use, as a first step in their potential applications we established both their physicochemical performance in ROS generation by EPR and also whether the resulting constructs operate within a safe biological window. The X-ray diffraction (XRD) pattern of the synthesized nanoparticles showed two distinct phases of iron oxides, wüstite (FeO, space group $Fm\bar{3}m$) and magnetite (Fe_3O_4, space group $Fd\bar{3}m$). Relative amounts of phases were 27% and 73% and estimated grain sizes of ~6.9 nm and ~2.4 nm, for FeO and Fe_3O_4, respectively. A quantitative refinement of these phases by the Rietveld method (Figure 1) was done using two models. In the first, no coupling between the phases was considered, and the lattice parameter of FeO (4.2079 Å) was found to be half of the lattice parameter of Fe_3O_4 (8.4050 Å). A second approach, with a coupling between the phases introduced in the refinement, yielded a shared microstrain parameter of ~0.25% (see Table S1 in Supplementary Material). These results indicate that the FeO@Fe_3O_4 MNPs are composed of two coupled phases, with Fe_3O_4 governing the overall crystalline framework, as inferred from the bulk lattice parameter (8.3941 Å).[21] The structural predominance of Fe_3O_4 results in a lattice distortion of the FeO component, whose parameter departs by 2.3% from the bulk value (4.301 Å).[22,23]

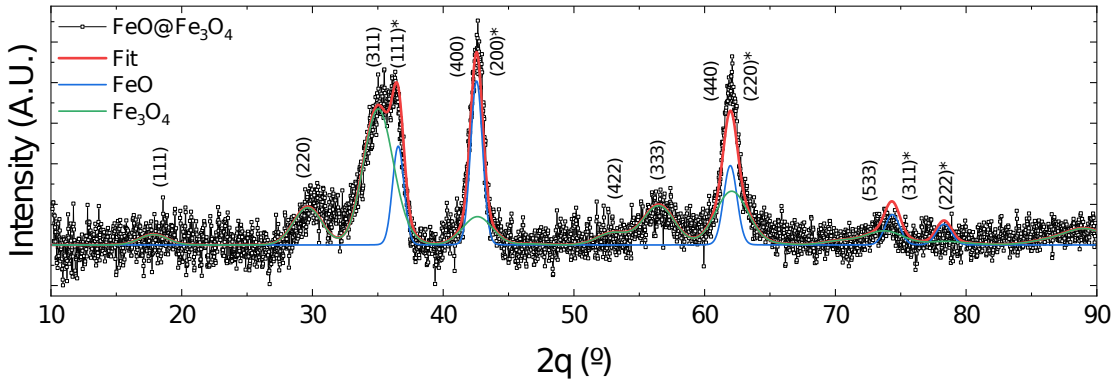

Figure 1. X-ray diffraction (XRD) pattern of synthesized FeO@Fe_3O_4 nanoparticles. The raw experimental data is shown in black. The Rietveld refinement fits for the wüstite (FeO) and magnetite (Fe_3O_4) phases are displayed in blue and green, respectively. The red line represents the combined Rietveld fit of both phases, showing its agreement with the raw data.*

Bright field TEM micrographs (Figure 2a) allowed for the determination of the morphology and size distribution of the synthesized MNPs. The size histogram, fitted with a log-normal function, yielded a mean diameter ⟨d⟩=9.6(5) nm; thus, the system can be considered as monodisperse (σ<10%). The determined value was consistent with the grain size estimated by Rietveld refinement when considering biphasic nanoparticles.

Electron diffraction patterns (Figure 2b) revealed rings indexed to an $Fm\bar{3}m$ structure, characterized of the FeO phase.[24] While the {111} reflections of the $Fd\bar{3}m$ structure (Fe_3O_4) identified in X-ray data[25] were not distinctly resolved in the selected area electron diffraction (SAED) patterns due to overlapping interplanar distances and the phase coupling suggested by Rietveld refinement, HRTEM provide two representative conditions to resolve the heterostructure: i) The core oriented in a Bragg condition (Figure 2c-d) displayed lattice fringes (2.4 Å) corresponding to the (111) planes of FeO, while the shell remained off-Bragg, allowing for an estimation of the core radius (~2.7 nm) and shell thickness (~2.7 nm) for an individual nanoparticle. In

contrast, oriented shell (Fe_3O_4) into Bragg condition (Figure 2e-f), lattice fringes (2.9 Å) corresponding to the (220) planes were resolved. These local structural observations confirmed the core-shell architecture, which is further validated by the magnetic exchange bias effect (Figure S2), a characteristic fingerprint of the ferrimagnetic-antiferromagnetic coupling at the Fe_3O_4/FeO interface.

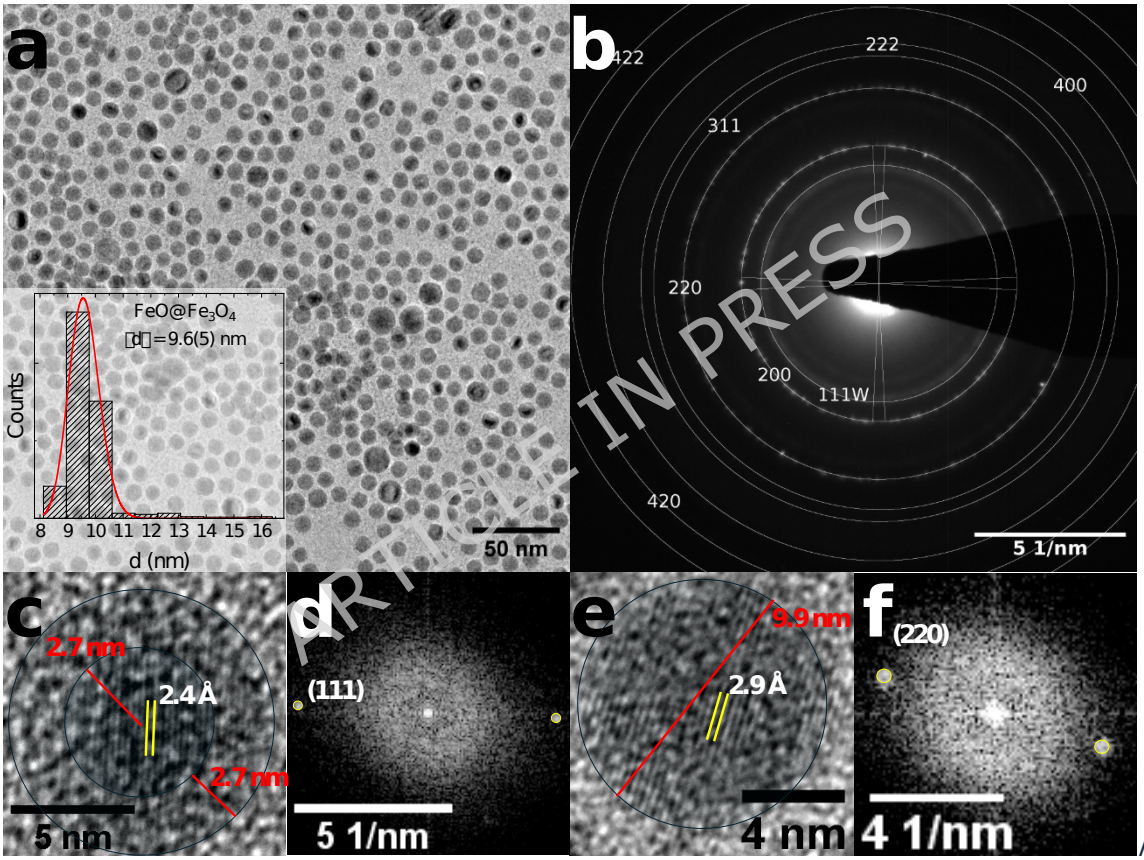

Figure 2. Transmission electron microscopy (TEM) characterization of synthesized FeO@Fe_3O_4 nanoparticles. Panel a: Bright-field TEM micrograph; the inset shows the size distribution histogram with a log-normal fit (9.6(5) nm). Panel B: Selected area electron diffraction (SAED) pattern with rings indexed to the $Fm\bar{3}m$ (FeO) and $Fd\bar{3}m$ (Fe_3O_4) phases. Panel c-d: HRTEM image (c) and corresponding FFT (d) of a single nanoparticle with core in Bragg condition, while the shell remains off-Bragg. Panel (e-f) HRTEM image (e) and corresponding FFT of a nanoparticle with the shell in Bragg condition (core off-Bragg).

Nanoparticle Coating

The presence of a glucose coating on the $FeO@Fe_3O_4$ MNPs after functionalization was assessed through Fourier Transform Infrared (FTIR) spectroscopy (Figure 3). The spectrum of the 'naked', non-coated MNPs taken for comparative purposes showed the characteristic C-H stretching vibrations at 2921 cm^{-1} and 2852 cm^{-1}, alongside a prominent 1538 cm^{-1} band indicative of surface-bound carboxylate from oleic acid,[26,27] as expected from the synthesis route. For the glucose-coated MNPs, the strong absorption band at 1012 cm^{-1} (C-O stretching) was evident, closely matching the corresponding band of pure glucose. This strong correlation of both spectra confirmed the attachment of glucose to the nanoparticle surface with good efficiency. Also, the C-H stretching vibrations in the 2900 cm^{-1} region could still be observed, probably associated with the glucose coating as evidenced by their similarity to the pure glucose spectrum. Moreover, the functionalized MNPs exhibited those additional absorption bands characteristic of glucose, including a very broad O-H stretching band centered around 3280 cm^{-1} and broader C-H stretching vibrations at 2923 cm^{-1} and 2854 cm^{-1}.[27] The broad absorption bands below 600 cm^{-1} could be assigned to the Fe-O stretching vibrations of the MNPs cores.[28]

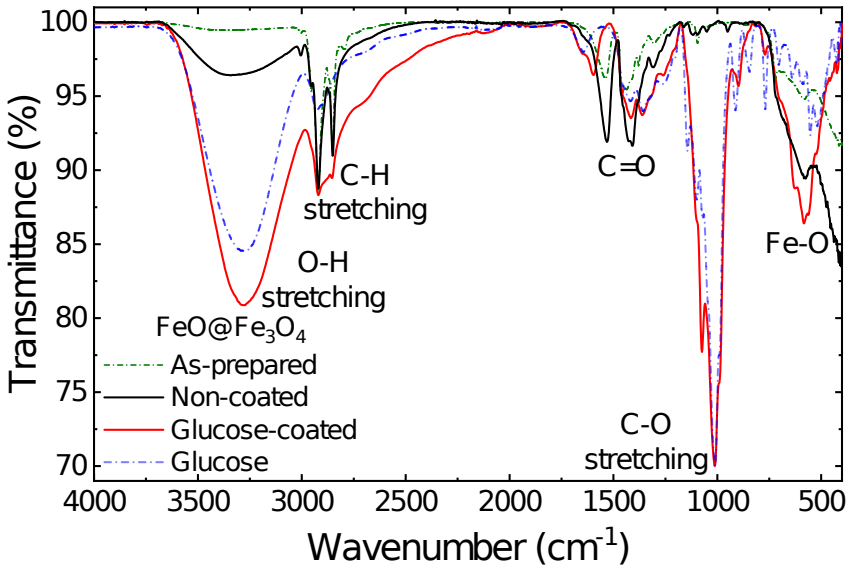

Figure 3. Fourier Transform Infrared (FTIR) spectra comparing non-coated and glucose-coated $FeO@Fe_3O_4$ nanoparticles. The non-coated $FeO@Fe_3O_4$ nanoparticles (black line) and after glucose coating (red line) were normalized to 2921 cm^{-1} C-H asymmetric stretching peak. The dark green and blue dashed lines *provide a reference spectrum of the* as-prepared nanoparticles *and* pure hydrated glucose*. The "non-coated" designation refers to particles that have undergone a cleaning procedure to remove the organic surfactant from "as-prepared" nanoparticles.*

Colloidal Properties

The size, polydispersity, and interparticle interactions of the glucose-coated $FeO@Fe_3O_4$ nanoparticles in solution were studied through Small-Angle X-ray Scattering (SAXS) (Figure S5). The fitting results yielded a mean radius ⟨d⟩=5.957(4) nm and polydispersity s=0.0794(9) when considering only a sphere form factor. Both parameters are consistent with the TEM-derived $FeO@Fe_3O_4$ mean diameter and polydispersity (σ<10%), suggesting a glucose shell thickness of about ~1.2 nm. However, the initial approach failed in the high-Q region, and fitting the full Q-range with many free parameters introduced strong correlations. Fixing the polydispersity from the sphere form-factor fit and using a square-well structure factor (parameters summarized in Table S2 of Supplementary Material) markedly improved the full-range fit, yielding a mean radius of 6.031(3) nm, still consistent with TEM and the initial

SAXS estimate. The resulting parameters also indicated an attractive interparticle interaction among the glucose-coated nanoparticles in solution, with well-width parameters, suggesting that this attraction extends for approximately 60% of the particle's radius beyond its surface.

EPR Evidence for Fenton-Like Radical Pathways

Spin-trapping EPR spectroscopy was performed to identify reactive oxygen species generated by glucose-coated $FeO@Fe_3O_4$ nanoparticles at pH 5 and in water, and by non-coated $FeO@Fe_3O_4$ nanoparticles at pH 5 (Figure S6 in the Supplementary Material). In the blank control (i.e., without nanoparticles), low concentrations of •OH radicals were observed, with negligible •OOH radicals (Figure 4B). As expected for Fenton-like reactions mediated by the Fe^{2+} ion, the non-coated nanoparticles led to a significant increase in •OH radical concentration, approaching 15 pM after 60 min.

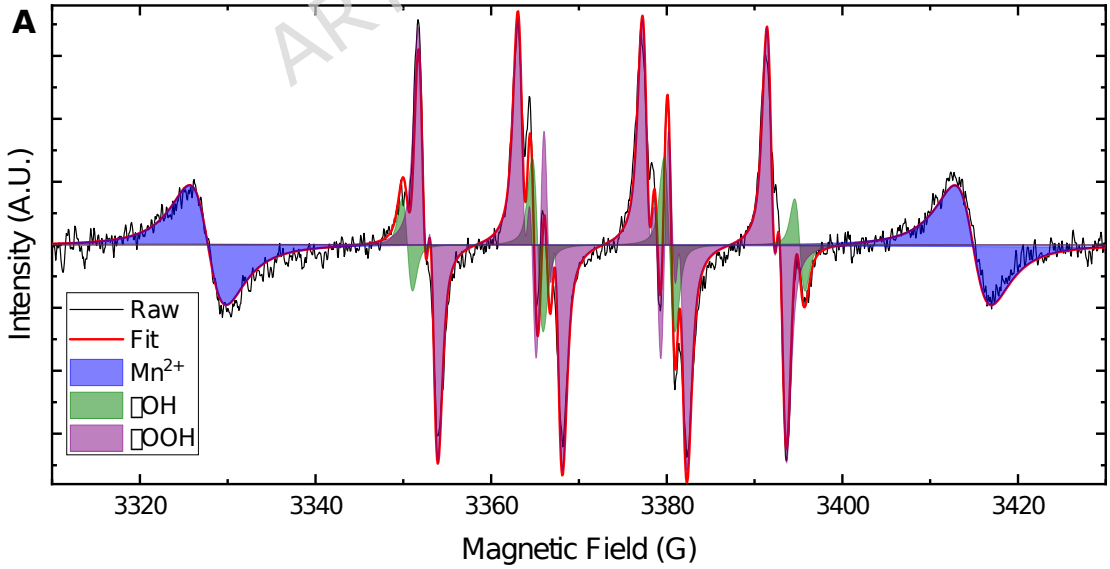

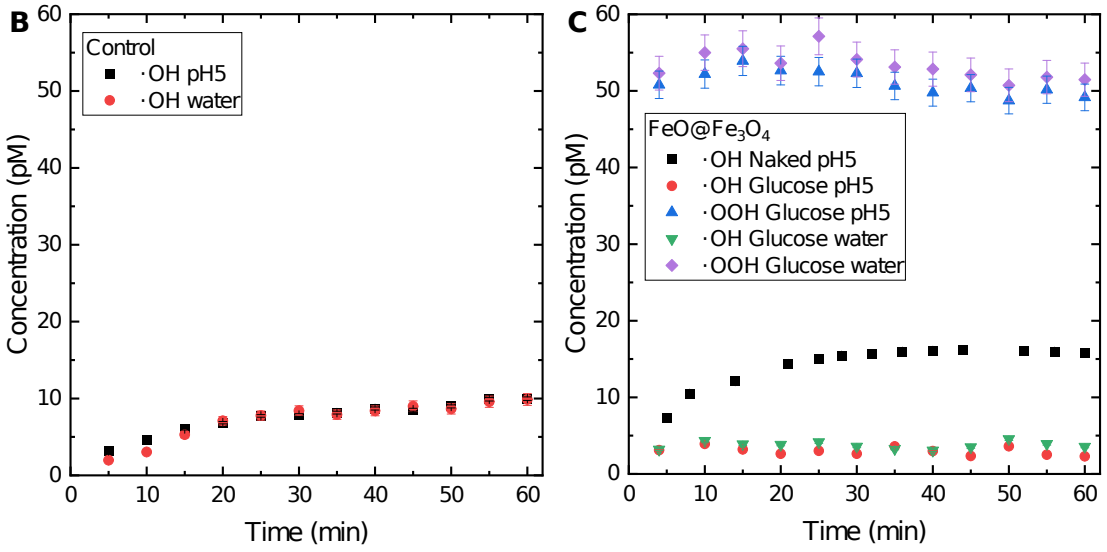

Figure 4. A: EPR spectrum (black line) of DMPO-adducts after exposure of the nanoparticles to H_2O_2 in water. The raw data is fitted (red line) to contributions from hydroxyl radicals (DMPO-•OH, green area) and hydroperoxyl radicals (DMPO-•OOH, violet area). A Mn^{2+} standard (blue area) is included for DMPO-adducts' quantification. The estimated concentration of hydroxyl and hydroperoxyl radicals as a function of time in the control (i.e., without nanoparticles) (B), and the time-dependent radical generation in nanoparticle-containing samples (C).

In contrast, the glucose-coated nanoparticles significantly suppressed the generation of •OH radicals (below 5 pM) and instead led to a sustained increase in the concentration of •OOH radicals (Figure 4C), reaching a peak of approximately 55 pM before slowly decaying over 60 min. These results suggest that the glucose coating is actively influencing the radical generation mechanism by acting as a scavenger of the highly reactive •OH radicals, promoting a dominant pathway towards the generation of •OOH species. For comparison, pure Fe_3O_4 nanoparticles of similar size and synthesis origin exhibit a predominant production of •OH radicals in their non-coated state (Figure S7 in the Supplementary Material); however, upon glucose coating, the radical output shirts toward •OOH, while maintaining the characteristic kinetics decay of magnetite.

The above data indicate that $FeO@Fe_3O_4$ MNPs are controllable oxidative nano-reactors. The coupled FeO/Fe_3O_4 biphasic architecture provides accessible Fe^{2+}/Fe^{3+} redox couples required for peroxide activation, whereas glucose functionalization strongly attenuates •OH and shifts the radical output toward •OOH. This effect may arise from ligand-mediated scavenging of surface-bound •OH and/or from a reduction in interfacial Fe-site accessibility, as commonly reported for coated iron-oxide nanozymes. This rerouting of radical speciation is relevant for biomedical use because •OH is highly reactive and diffusion-limited, whereas •OOH/$•O_2^-$ participates in longer-lived redox cycles. Moreover, the modest DMPO-adduct levels observed under our assay conditions are consistent with catalytic activity being retained while the most damaging radical channel is suppressed, in the absence of detectable lipid peroxidation and genotoxicity under the tested conditions.

Although the present study examined only glucose as the surface ligand, the rerouting of radical speciation is not expected to be unique to this molecule. In the case of glucose, the literature suggests that carbohydrate oxidation is promoted by •OH generated at Fe^{2+} sites, and that this oxidation is strongly reduced by the addition of •OH radical scavengers or Fe^{2+}-chelating agents.[29] This process involves the formation of a glucose peroxyl radical intermediate, which can subsequently release •OOH radicals into the solution[30]. More generally, surface ligands can alter peroxide access to Fe sites, modulate interfacial electron transfer, and scavenge short-lived radicals, thereby shifting the relative •OH/•OOH output. In this context, other coordinating or

hydrophilic ligands, such as carboxylates or polysaccharides, may also modify the radical pathway, although the direction and magnitude of the effect will depend on ligand binding strength, surface density, and redox activity. For instance, it has been reported that organic acids or alcohol groups can produce carbon-centered radicals in presence of •OH generated from Fe^{2+} sites.[31] Our data therefore support a ligand-dependent, rather than glucose-exclusive, control of radical speciation; systematic comparison among ligands lies beyond the scope of the present work.

Safety evaluation of $FeO@Fe_3O_4$ nanoparticles

Nanoparticle interaction with Spheroids

The MNP penetration's profile into 3D spheroids was assessed through a reconstruction from a sequential ~35–40 TEM images acquired along the spheroid cross-section was performed. A high-magnification reconstruction of an untreated control spheroid is provided in Figure S9 of the supplementary material to serve as a baseline for the intact spheroid architecture. Following 24-hour exposure to glucose-coated $FeO@Fe_3O_4$ MNPs, a low-magnification cross-section (~120 µm) of the exposed spheroid showed a clear preferential accumulation of NP clusters at the spheroid rim (Figure 5, upper panel). Higher-magnification images were then analyzed qualitatively to identify localization patterns in the examined sections. A major fraction of the MNPs was found forming clusters at the spheroid surface, consistent with the densely packed rim acting as a barrier to penetration (Figure 5d). However, also transcellular uptake with morphological alterations in the periphery was

observed (Figure 5a) and, within this region, MNPs were found confined to membrane-bound vesicles (endosomes), consistent with endocytosis. A main fraction of the internalized MNPs were detected distributed at 7-10 µm depth from the rim, defining the initial penetration zone. Deeper inside penetration was scarce (Figure 5b,c): few MNPs were observed at ≈10-15 µm (Figure 5c) and exceptionally at »30-35 µm (Figure 5b) from the rim. In Figure 5c, MNPs lie in intercellular spaces, indicative of paracellular transport, whereas in Figure 5b they appear in the cytosol without visible endosomal membranes, suggesting either non-endocytic entry or post-endocytic endosomal escape. The deepest penetration co-localizes with regions showing greater morphological damage, suggesting an association between MNP exposure and compromised cellular integrity.

From this single-spheroid dataset, we identify three modes of NP localization: (i) adsorption at the spheroid surface (rim), (ii) presence in intercellular clefts consistent with paracellular transport, and (iii) intracellular localization via transcellular uptake, the latter resolved into endosome-confined and cytosolic populations. The images also showed penetration to defined depths and a spatial co-occurrence between deeper NP presence and increased peripheral morphological damage, suggesting a possible association of these two effects. Considered together with the NP surface chemistry, the data are compatible with the hydrophilic glucose shell favoring interaction with the spheroid periphery and allowing both intercellular and intracellular localization. These TEM observations are qualitative and limited to the analyzed sections under a

single exposure condition; they describe localization patterns and penetration depths, but do not quantify the amount of nanoparticles internalized within spheroids or establish uptake efficiency at the population level. Although MNPs appear as clusters (consistent with SAXS indications of attractive interparticle interactions), the glucose coating likely reduces nonspecific protein fouling that would otherwise promote larger, immobilizing aggregates.[32]

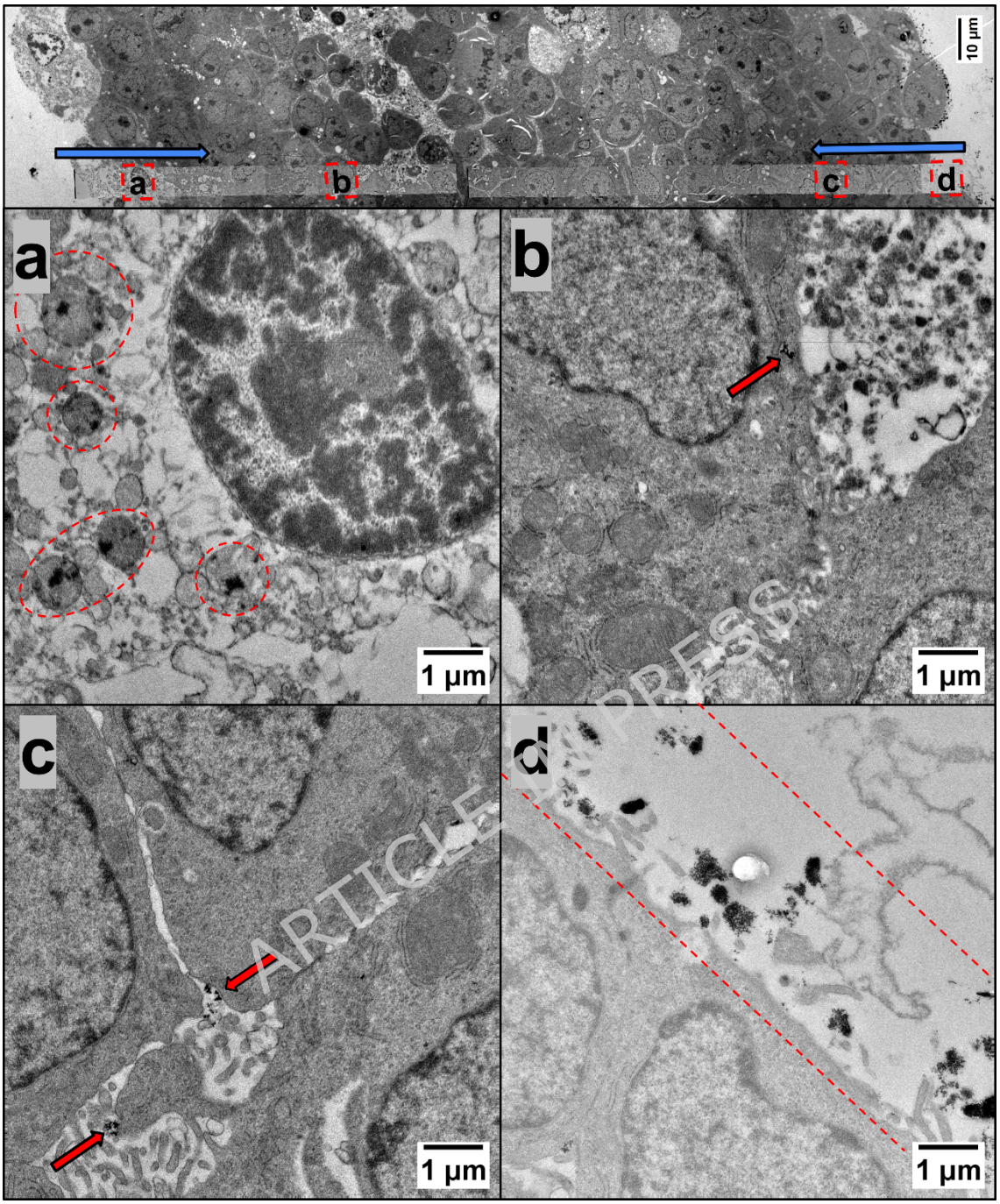

Figure 5. Transmission electron microscopy (TEM) images showing the qualitative localization of glucose-coated FeO@Fe_3O_4 nanoparticles across HepG2 spheroid cross-sections after 24 h exposure. The top panel provides a panoramic overview of the spheroid cross-section, with blue arrows indicating the outward-to-inward direction of MNP uptake. Panels a–d show higher-magnification regions in which nanoparticles were observed. Nanoparticles are highlighted by red dashed circles (a), red arrows (b, c), and red dashed lines (d).

Cyto and Genotoxiciy of the $FeO@Fe_3O_4$ nanoparticles

Potential adverse effects (cyto and genotoxicity) of $FeO@Fe_3O_4$ MNPs were evaluated using an advanced human hepatic *in vitro* model, HepG2 spheroids (Figure S8), which offers a compelling alternative to traditional monolayer cultures by enhancing cell–cell interactions and better preserving liver-specific functions, such as the expression of metabolic enzymes. As a result, it more closely mimics *in vivo* hepatic conditions.[33] Furthermore, the HepG2 cell line is widely used as an *in vitro* model for toxicological studies due to its expression of the wild-type p53 tumor suppressor protein and its retained activity of various xenobiotic-metabolizing enzymes.[34]

The cytotoxicity of the tested $FeO@Fe_3O_4$ MNPs was assessed using the CellTiter-Glo Assay. As shown in Figure 6, cell viability decreased in a dose- and time-dependent manner following 24 and 96 hours of exposure. Notably, after 96 hours, a more pronounced cytotoxic effect was observed even at lower concentrations, indicating increased sensitivity with prolonged exposure. Furthermore, after 24 hours of exposure, an IC_{50} value was 29.3 $\mu g/cm^2$, while after 96 hours the IC_{50} value decreased to approximately 10.8 $\mu g/cm^2$.

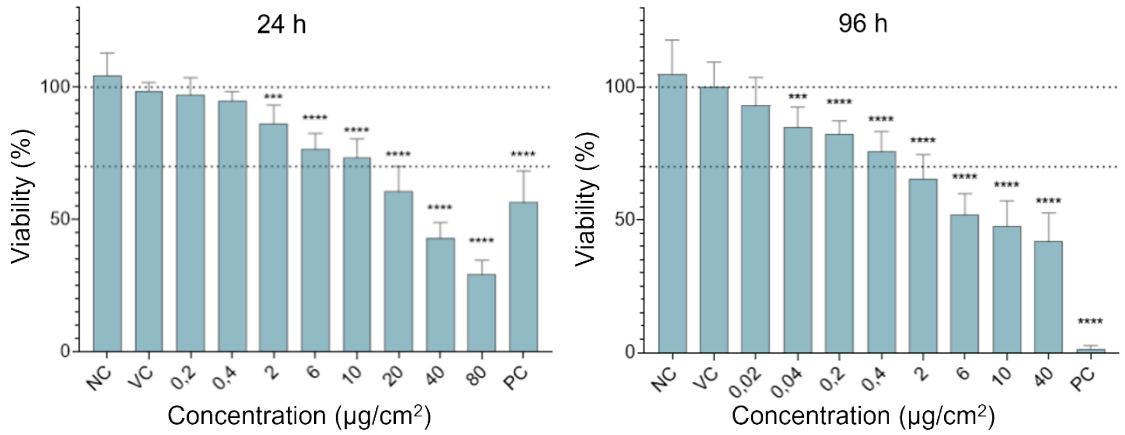

*Figure 6. Cytotoxicity of glucose-coated FeO@Fe_3O_4 MNPs for HepG2 spheroids. Cell viability was measured by using the CellTiter-Glo assay. The panels show cell viability after 24- and 96-hour exposure to graded concentrations of the nanoparticles (0.2 to 80 µg/cm² and 0.02 to 40 µg/cm², respectively). Data is presented relative to the vehicle control (VC; up to 3% Milli-Q water in cell media). NC – cell culture media, PC - 15% DMSO. **** denotes statistically significant difference between the vehicle control and MNPs exposed cells, ANOVA; Dunnett's Multiple Comparison test, ***P < 0.001, ****P < 0.0001).*

The surfaces of iron oxide nanoparticles are known to be capable of catalytically generating reactive oxygen species (ROS) through the Fenton and Haber-Weiss reactions,[35] consequently leading to oxidative stress.[36] Physico-chemical characterization of FeO@Fe_3O_4 MNPs showed that the tested nanoparticles are capable of free radical generation, which may react with different cellular macromolecules, such as DNA, cell membranes or proteins, eventually leading to different pathological and toxicological processes.[37] In our study, malondialdehyde (MDA) was measured as a marker of lipid peroxidation, since it is one of the most frequently used biomarkers of oxidative stress.[38] The results (Figure 7) showed no significant increase in MDA formation in a concentration range up to 20 µg/cm² at 4 or 24 hours of exposure. Tested concentrations were determined based on the results of the cell viability assay in a way that the highest tested concentration did not decrease cell viability by more than 25-30 %.

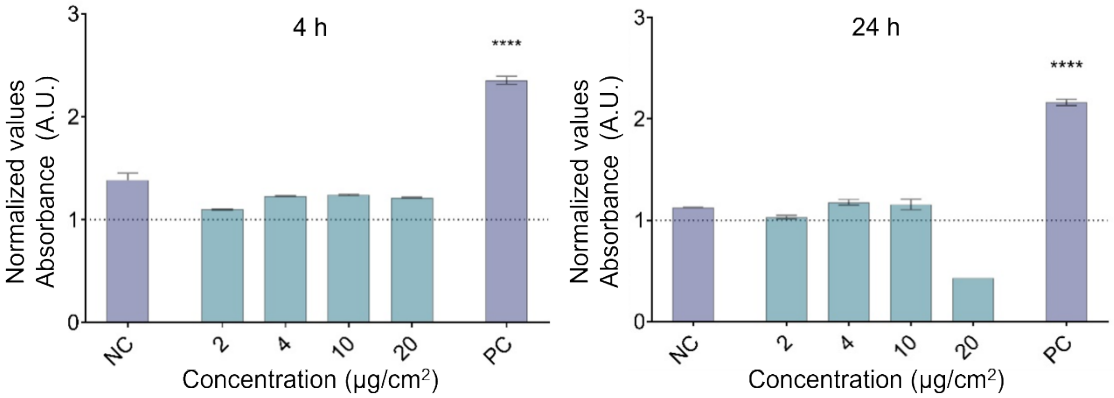

*Figure 7. MDA formation after exposure to glucose-coated FeO@Fe_3O_4 MNPs in HepG2 spheroids. MDA was measured by the Lipid Peroxidation (MDA) Assay Kit. The panels show MDA levels after a 4- and 24-hour exposure to graded concentrations of the nanoparticles (from 2 to 20 μg/cm^2). The results are expressed as the normalized values to vehicle control (VC; up to 3% Milli-Q water in cell media), marked as a dotted line. NC is the negative control (media), and PC is the positive control (1 mM tert-Butyl hydroperoxide; tBOOH, 4 h). A statistically significant difference (ANOVA and Dunnett's post-test) between MNPs-exposed cells and the VC is indicated by ****P < 0.0001.*

Potential DNA damage at the level of individual cells was evaluated using single-cell gel electrophoresis (SCGE), commonly known as the comet assay. This assay is capable of detecting various forms of DNA damage, including single- and double-strand breaks (SSBs and DSBs), alkali-labile sites such as apurinic/apyrimidinic (AP) sites, DNA-DNA and DNA-protein cross-links, oxidized and alkylated bases, UV-induced cyclobutane pyrimidine dimers, and certain chemically induced DNA adducts.[39,40] Furthermore, it can detect transient SSBs that appear during DNA damage repair.[41] Exposure of HepG2 spheroids to graded concentrations of FeO@Fe_3O_4 MNPs (up to 10 μg/cm^2) resulted in no significant increase in DNA damage, as shown in Figure 8.

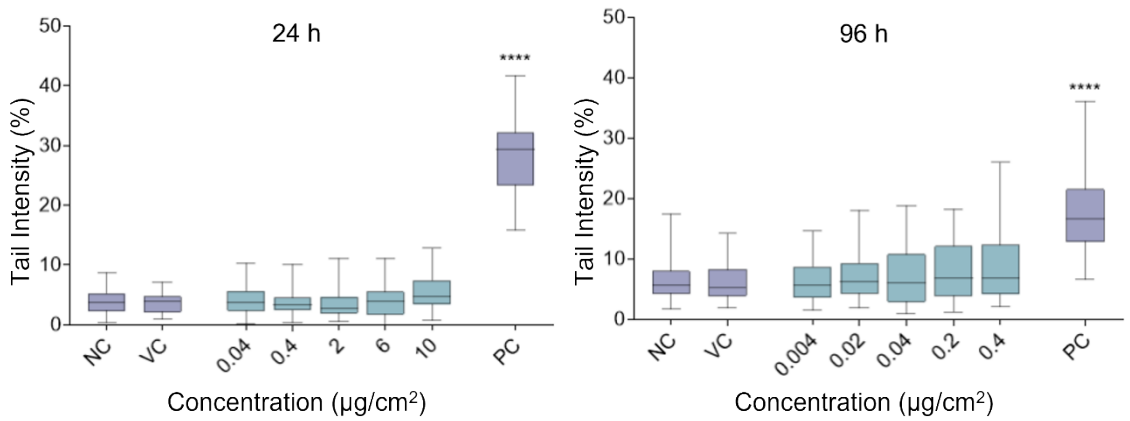

*Figure 8. Potential DNA damage induction by glucose-coated FeO@Fe_3O_4 MNPs in HepG2 spheroids. DNA damage was assessed by using the comet assay, measuring the percentage of DNA in the comet tail. The panels show results after 24- and 96-hour exposure to graded concentrations of the nanoparticles (0.04 to 10 µg/cm² and 0.004 to 0.4 µg/cm², respectively). Data are presented as quantile box plots. The edges of the box represent the 25th and 75th percentiles, the median is a solid line through the box, and the error bars represent 95% confidence intervals. PC is the positive control (30 µM and 5 µM BaP for 24 and 96 h, respectively). A statistically significant difference (Kruskal-Wallis and Dunn's post-test) between MNPs-exposed cells and the vehicle control (VC; up to 3% Milli-Q water in cell media) is indicated by ****P < 0.0001.*

To verify that the tested FeO@Fe_3O_4 MNPs do not induce DNA DSB or exhibit aneugenic activity, further evaluation was performed using immunofluorescent labelling of the DSB biomarker gH2AX and the aneugenicity marker phospho-histone H3 (p-H3), followed by flow cytometric analysis.

DNA DSBs trigger the rapid phosphorylation of histone H2AX, a component of the nucleosomal histone octamer. The phosphorylated form, gH2AX, accumulates at DSB sites, forming nuclear foci that correlates directly with the extent of DNA damage. This makes gH2AX a well-established biomarker for DSB induction and clastogenic activity.[42] Similarly, histone H3 becomes phosphorylated during mitosis to facilitate chromosome condensation and segregation. Since aneugenic compounds can induce this phosphorylation, p-H3 serves as a reliable biomarker for mitotic activity and aneugenic effects.[43]

Analysis of the induction of DNA DSBs and p-H3-positive events after exposure to the tested FeO@Fe_3O_4 MNPs confirmed that none of them induced the formation of DSBs (Figure 9A), nor increased the percentage of p-H3-positive events (Figure 9B), at any of the concentrations tested.

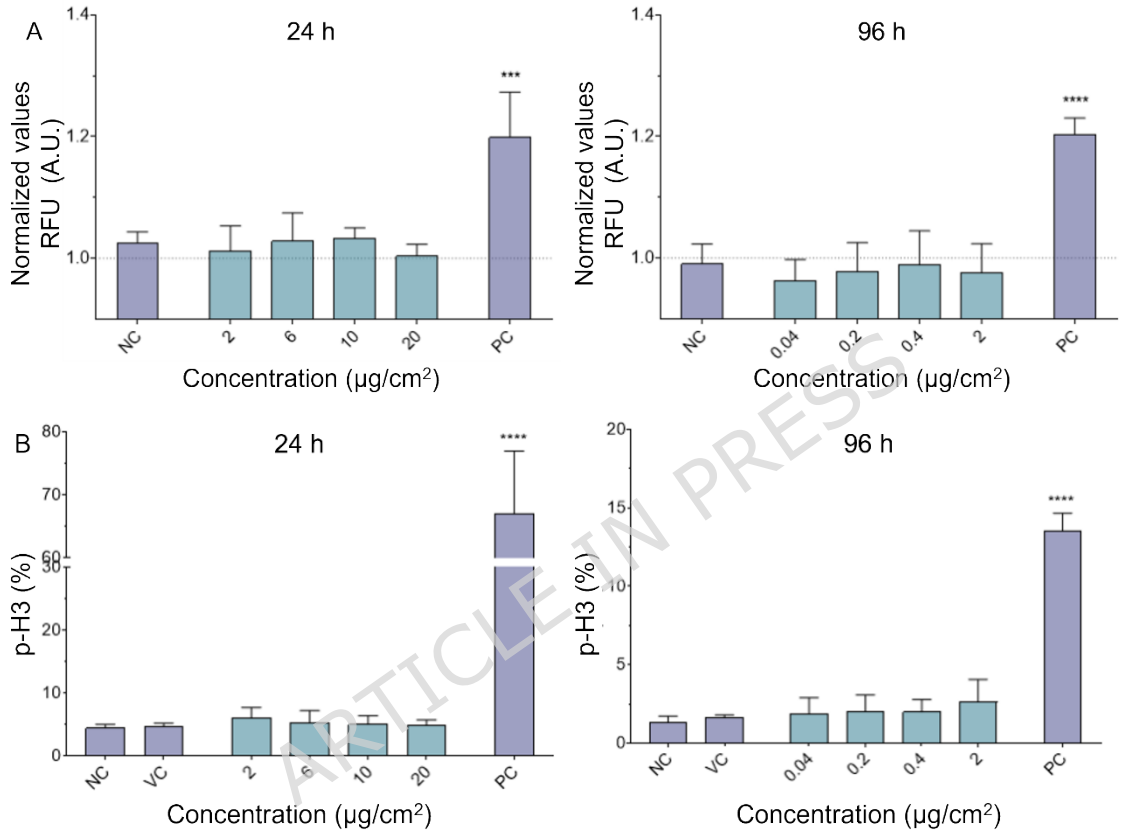

*Figure 9. Potential induction of DNA double-strand breaks (DSBs) and p-H3 positive events by glucose-coated FeO@Fe_3O_4 MNPs in HepG2 spheroids. A) The fluorescence intensity of γH2AX was measured in individual cells by flow cytometry and normalized to the vehicle control (VC; up to 3% Milli-Q water in cell culture media), represented by dotted line. Cells were exposed to increasing concentrations of the nanoparticles for 24 hours (up to 20 µg/cm²) and 96 hours (up to 2 µg/cm²). Etoposide (1.7 µM) served as a positive control (PC). Statistically significant differences between MNPs–treated cells and the VC were determined using ANOVA, followed by Dunnett's post-test and are indicated as ****P < 0.0001. B) The average percentage of p-H3–positive events, indicative of mitotic activity, was also determined by flow cytometry following exposure to graded concentrations of the nanoparticles for 24 hours (up to 20 µg/cm²) and 96 hours (up to 2 µg/cm²). Colchicine (0.1 µM) was used as a positive control. Significant differences compared to the VC (up to 3% Milli-Q water in cell media) were identified by ANOVA and Dunnett's post-test and are marked as ****P < 0.0001.*

The above description shows that the limited penetration depth observed for the FeO@Fe_3O_4 MNPs could be connected to the low genotoxicity observed.[44] Namely, the average spheroid diameter of ~320 µm (Figure S8) implies a

medium spheroid volume of ~1.7×10^7 μm^3. A very approximate estimation yields a number of ~2.6×10^4 cells/spheroid. The penetration depth observed from TEM of 7-10 mm implies that the volume of the rim accessible to nanoparticles is ≈7-9×10^5 mm^3, i.e., ≈3-5×10^3 cells in the rim, which represents 12-17 %of the total spheroid volume. Thus, the majority of cells within the spheroid remain physically separated from the nanoparticles and are not directly exposed to them. It is known that, once nanoparticles are internalized through endocytic pathways, they can be transported through the endolysosomal network within membrane-bound vesicles by motor proteins and cytoskeletal elements.[45] This vesicular sequestration likely acts as a protective mechanism for the cell's core structures, limiting the nanoparticles' access to sensitive targets such as nuclear DNA. To reach cytoplasmic or nuclear components, nanoparticles must first escape the endolysosomal compartment; only then can they directly interact with genomic DNA.[46,47]

On the other hand, despite the low penetration observed, FeO@Fe_3O_4 MNPs exhibited dose- and time-dependent cytotoxicity. In general, several mechanisms may underline the cytotoxicity induced by iron-based nanoparticles. Extracellularly, iron-based nanoparticles can generate ROS that mechanically disrupt the plasma membrane by creating nanoscale pores, or bind to membrane proteins such as NADPH oxidase, Ca^{2+} channels, and various receptors. These interactions can trigger oxidative signaling pathways, elevate intracellular Ca^{2+} levels, and activate downstream second-messenger cascades. Additional intracellular mechanisms may include ROS generation

following internalization of those nanoparticles, lysosomal destabilization, disruption of the cytoskeleton through direct interactions with structural proteins, and the induction of protein conformational changes.[48] Nevertheless, once internalized, nanoparticles may interfere with mitochondrial metabolism, leading to impaired ATP production and activation of apoptotic pathways.[49–51] Since internalization of tested nanoparticles was limited in the present study, cytotoxicity may instead arise from the release of ions from these nanoparticles,[52] especially since no increase in MDA levels and no DNA damage was detected. Namely, ions released from MNPs and consequently iron overload could interfere with mitochondrial iron homeostasis[53] and electron transport, impairing energy metabolism and leading to metabolic failure before the onset of widespread lipid peroxidation.[54,55] Such mitochondrial impairment may represent an early event in iron-dependent cell death pathways, such as ferroptosis, which can be initiated by iron dysregulation and localized redox imbalance before detectable changes in oxidative stress markers, such as MDA.[56]

While a complete determination of the exact mechanisms underlying the observed cytotoxicity is beyond the scope of this work, we would like to emphasize that, although certain aspects of nanoparticle toxicity can be reasonably predicted using *in vitro* assays, it remains challenging to determine whether the detected cytotoxic responses are truly indicative of clinically relevant effects. The absence of genotoxic activity observed in our system is a fundamental step since genotoxicity poses a major barrier to clinical

translation. Still, the dose- and time-dependent cytotoxicity observed highlights the need to carefully assess exposure limits and underscores the importance of balancing therapeutic benefit with potential off-target effects.

Moreover, the absence of detectable genotoxicity, despite the radical-generating capacity demonstrated by EPR, can be discussed in light of the observed TEM localization patterns. In the analyzed sections, MNPs were predominantly found at the spheroid periphery and frequently within membrane-bound vesicles, which may reduce direct access to nuclear DNA. Sparse cytosolic events were also observed, but the present data do not allow inference about their downstream intracellular consequences. Accordingly, the TEM observations provide a plausible qualitative explanation for the lack of genotoxicity, although they cannot be considered conclusive regarding the intracellular origin of the ATP decline or on localized oxidative processes within specific compartments.

Conclusions

The present work showed that FeO@Fe_3O_4 core–shell MNPs with a glucose coating displayed sustained redox activity, while their hydrophilic coating nature enabled penetration through intercellular spaces and cellular uptake. A tightly coupled biphasic lattice (27% FeO / 73% Fe_3O_4) architecture selectively catalyzed hydroperoxyl formation (>50 pM •OOH in 10 min) under near-physiological conditions, outpacing hydroxyl production. These MNPs produced a dose- and time-dependent cytotoxicity (IC_{50} ≈10.8 μg/cm², 96 h)

without significant lipid peroxidation in HepG2 spheroids. Cross-sectional spheroid images analyzed by TEM showed that MNPs were able to penetrate to ≈10–15 mm, therefore delineating an essentially one-cell-thick peripheral rim where most MNPs accumulated, with only sparse particles deeper in the tissue (up to ~30 mm from the spheroid surface). This internalization behavior provides a plausible explanation for the absence of genotoxicity by protecting the cell's core structures from direct damage. The lack of lipid peroxidation indicates no severe oxidative stress after exposure to the MNPs. This suggests that the cytotoxicity, observed as an ATP decline, originated from a different mechanism. Although the present data do not establish the underlying intracellular pathway, they are compatible with mitochondrial dysfunction. Our results suggest a clear structure–activity relationship: the redox-active Fe^{2+} in $FeO@Fe_3O_4$ modulates Fenton-like catalysis, and the glucose coating governs colloidal stability, cellular uptake and spheroid penetration. These findings represent a safe operational window in which $FeO@Fe_3O_4$ nano-reactors can deliver controlled oxidative effects without off-target genotoxicity, supporting their further development as remotely activatable catalysts for oxidative nanomedicine and other biologically integrated redox applications.

Acknowledgements

M.A.M.O. thanks Dr. D. Zákutná and MultiFUN group for their hospitality and supervision at Charles University, and Dr. Milan Dopita from Math and Physics Faculty for facilitating SAXS data acquisition. We are grateful to M. Soriano for

helpful discussions and for the preparation of biological samples for TEM analysis.

Funding

This research was funded by H2020-MSCA NESTOR project (101007629), the HE CutCancer project (101079113), ARIS P1-0245, ARIS J1-4395, ARIS MR grant to IR. E.L. and E.L.W: acknowledge financial support from PICT-2019-02059.

Conflicts of interest

The authors declare there are no conflicts of interest.

Data availability

The datasets generated and analyzed during the current study are available in the Zenodo repository, https://zenodo.org/records/18205062. Additional data (or any materials not included in the repository) are available from the corresponding author upon reasonable request.

References

1. Santos, L. F. *et al.* Remote-Controlled Magnetic Stimulation of Cell-Based Bioengineered Tissues for In Situ Bone Regeneration. *Advanced Materials* **37**, 2500657 (2025).

2. Falconieri, A. *et al.* Magnetically-actuated microposts stimulate axon growth. *Biophys. J.* **121**, 374–382 (2022).

3. De Jong, W. H. & Borm, P. J. *Drug Delivery and Nanoparticles: Applications and Hazards*. *International Journal of Nanomedicine* vol. 3 https://www.dovepress.com/ (2008).

4. Han, X., Xu, K., Taratula, O. & Farsad, K. Applications of nanoparticles in biomedical imaging. *Nanoscale* vol. 11 799–819 Preprint at https://doi.org/10.1039/c8nr07769j (2019).

5. Chen, J. *et al.* Immuno gold nanocages with tailored optical properties for targeted photothermal destruction of cancer cells. *Nano Lett.* **7**, 1318–1322 (2007).

6. Zheng, C. *et al.* Redox-Activatable Magnetic Nanoarchitectonics for Self-Enhanced Tumor Imaging and Synergistic Photothermal-Chemodynamic Therapy. *Small Methods* **8**, 2301099 (2024).

7. Huo, M., Wang, L., Wang, Y., Chen, Y. & Shi, J. Nanocatalytic Tumor Therapy by Single-Atom Catalysts. *ACS Nano* **13**, 2643–2653 (2019).

8. Iroegbu, A. O. C., Teffo, M. L. & Sadiku, E. R. Cancer therapy with engineered nanozymes: from molecular design to tumour-responsive catalysis. *Nanomedicine* **20**, 1799–1817 (2025).

9. Havelikar, U. *et al.* Comprehensive insights into mechanism of nanotoxicity, assessment methods and regulatory challenges of nanomedicines. *Discover Nano 2024 19:1* **19**, 165- (2024).

10. Gao, L. *et al.* Intrinsic peroxidase-like activity of ferromagnetic nanoparticles. *Nature Nanotechnology 2007 2:9* **2**, 577–583 (2007).

11. Zheng, J. J. *et al.* Optimizing the standardized assays for determining the catalytic activity and kinetics of peroxidase-like nanozymes. *Nature Protocols 2024 19:12* **19**, 3470–3488 (2024).

12. Bowen, H. K., Adler, D. & Auker, B. H. *Electrical and Optical Properties of FeO**. *JOURNAL OF SOLID STATE CHEMISTRY* vol. 12 (1975).

13. Calhount, B. A. *Magnetic and Electric Properties of Magnetite at Low Temperatures**. vol. 94 (1954).

14. Shokrollahi, H. A review of the magnetic properties, synthesis methods and applications of maghemite. *Journal of Magnetism and Magnetic Materials* vol. 426 74–81 Preprint at https://doi.org/10.1016/j.jmmm.2016.11.033 (2017).

15. Sieg, H. *et al.* Particulate iron oxide food colorants (E 172) during artificial digestion and their uptake and impact on intestinal cells. *Toxicology in Vitro* **96**, 105772 (2024).

16. Pereira, M. C., Oliveira, L. C. A. & Murad, E. Iron oxide catalysts: Fenton and Fentonlike reactions – a review. *Clay Miner.* **47**, 285–302 (2012).

17. Štampar, M., Tomc, J., Filipič, M. & Žegura, B. Development of in vitro 3D cell model from hepatocellular carcinoma (HepG2) cell line and its application for genotoxicity testing. *Arch. Toxicol.* **93**, 3321–3333 (2019).

18. *Study Report and Preliminary Guidance on the Adaptation of the In Vitro Micronucleus Assay (OECD TG 487) for Testing of Manufactured Nanomaterials*. (2022).

19. Francisco, S. & Francisco, S. γ-H2AX – A Novel Biomarker for DNA Double-strand Breaks. *In Vivo (Brooklyn).* **22**, (2008).

20. Recoules, C., Huertas, C., Vignard, J. & Audebert, M. Comparison of different techniques for γH2AX/pH3 biomarkers quantification for chemical genotoxicity assessment. *Mutat. Res. Genet. Toxicol. Environ. Mutagen.* **906**, 503878 (2025).

21. Fleet, M. E. The Structure of Magnetite. *Structural Science* **37**, 917–920 (1981).

22. Jette, E. R. & Foote, F. An x-ray study of the wüstite (FeO) solid solutions. *J. Chem. Phys.* **1**, 29–36 (1933).

23. Fjellvå, H., Grønvold, F., Stølen, S. & Hauback, B. *On the Crystallographic and Magnetic Structures of Nearly Stoichiometric Iron Monoxide*. *JOURNAL OF SOLID STATE CHEMISTRY* vol. 124 (1996).

24. Testa-Anta, M., Rodríguez-González, B. & Salgueiriño, V. Partial FeO–Fe3O4 Phase Transition Along the <111> Direction of the Cubic Crystalline Structure in Iron Oxide Nanocrystals. *Particle and Particle Systems Characterization* **36**, (2019).

25. Arndt, B. *et al.* Atomic structure and stability of magnetite Fe3O4(001): An X-ray view. *Surf. Sci.* **653**, (2016).

26. Aadinath, W. & Muthuvijayan, V. Influence of oleic acid coating on the magnetic susceptibility and Fenton reaction-mediated ROS generation by the iron oxide nanoparticles. *Nano Express* **5**, (2024).

27. Ibrahim, M., Alaam, M., El-Haes, H., Jalbout, A. F. & De Leon, A. Analysis of the structure and vibrational spectra of glucose and fructose. *Ecletica Quimica* **31**, (2006).

28. Petcharoen, K. & Sirivat, A. Synthesis and characterization of magnetite nanoparticles via the chemical co-precipitation method. *Materials Science and Engineering: B* **177**, 421–427 (2012).

29. Gutteridge, J. M. Reactivity of hydroxyl and hydroxyl-like radicals discriminated by release of thiobarbituric acid-reactive material from deoxy sugars, nucleosides and benzoate. *Biochem. J.* **224**, (1984).

30. Bothe, E., Schulte-Frohlinde, D. & Von Sonntag, C. Radiation chemistry of carbohydrates. Part 16.† Kinetics of HO 2 elimination from peroxyl radicals derived from glucose and polyhydric alcohols. *Journal of the Chemical Society, Perkin Transactions 2* https://doi.org/10.1039/p29780000416 (1978) doi:10.1039/p29780000416.

31. Park, J. S. B., Wood, P. M., Davies, M. J., Gilbert, B. C. & Whitwood, A. C. A kinetic and ESR investigation of Iron(II) oxalate oxidation by hydrogen peroxide and dioxygen as a source of hydroxyl radicals. *Free Radic. Res.* **27**, (1997).

32. Bashiri, G. *et al.* Nanoparticle protein corona: from structure and function to therapeutic targeting. *Lab on a Chip* vol. 23 1432–1466 Preprint at https://doi.org/10.1039/d2lc00799a (2023).

33. Štampar, M., Breznik, B., Filipič, M. & Žegura, B. Characterization of In Vitro 3D Cell Model Developed from Human Hepatocellular Carcinoma (HepG2) Cell Line. *Cells* **9**, (2020).

34. Waldherr, M. *et al.* Use of HuH6 and other human-derived hepatoma lines for the detection of genotoxins: a new hope for laboratory animals? *Arch. Toxicol.* **92**, 921–934 (2018).

35. Wydra, R. J., Oliver, C. E., Anderson, K. W., Dziubla, T. D. & Hilt, J. Z. Accelerated generation of free radicals by iron oxide nanoparticles in the presence of an alternating magnetic field. *RSC Adv.* **5**, 18888–18893 (2015).

36. Pizzino, G. *et al.* Oxidative Stress: Harms and Benefits for Human Health. *Oxid. Med. Cell. Longev.* **2017**, 8416763 (2017).

37. De Zwart, L. L., Meerman, J. H. N., Commandeur, J. N. M. & Vermeulen, N. P. E. Biomarkers of free radical damage: Applications in experimental animals and in humans. *Free Radic. Biol. Med.* **26**, 202–226 (1999).

38. Khoubnasabjafari, M., Ansarin, K. & Jouyban, A. Reliability of malondialdehyde as a biomarker of oxidative stress in psychological disorders. *Bioimpacts* **5**, 123–127 (2015).

39. Møller, P. *et al.* Minimum Information for Reporting on the Comet Assay (MIRCA): recommendations for describing comet assay procedures and results. *Nature Protocols 2020 15:12* **15**, 3817–3826 (2020).

40. Collins, A. *et al.* Measuring DNA modifications with the comet assay: a compendium of protocols. *Nat. Protoc.* **18**, 929–989 (2023).

41. Collins, A. R. The comet assay for DNA damage and repair: principles, applications, and limitations. *Mol. Biotechnol.* **26**, 249–261 (2004).

42. Bonner, W. M. *et al.* γH2AX and cancer. *Nature Reviews Cancer* vol. 8 Preprint at https://doi.org/10.1038/nrc2523 (2008).

43. Prigent, C. & Dimitrov, S. Phosphorylation of serine 10 in histone H3, what for? *J. Cell Sci.* **116**, (2003).

44. Chen, W. *et al.* Size-Dependent Penetration of Nanoparticles in Tumor Spheroids: A Multidimensional and Quantitative Study of Transcellular and Paracellular Pathways. *Small* **20**, (2024).

45. Shang, L., Nienhaus, K. & Nienhaus, G. U. *Engineered Nanoparticles Interacting with Cells: Size Matters*. http://www.jnanobiotechnology.com/content/12/1/5 (2014) doi:10.1186/1477-3155-12-5.

46. Maria, M. F. *et al.* Evaluating Nanoparticle-Induced Cytotoxicity: Mechanisms and Methods. *Nano Biomedicine and Engineering* vol. 17 Preprint at https://doi.org/10.26599/NBE.2025.9290129 (2025).

47. Shukla, R. K., Badiye, A., Vajpayee, K. & Kapoor, N. Genotoxic Potential of Nanoparticles: Structural and Functional Modifications in DNA. https://doi.org/10.3389/fgene.2021.728250 doi:10.3389/fgene.2021.728250.

48. nanomedicine, E. F.-I. journal of & 2012, undefined. The role of surface charge in cellular uptake and cytotoxicity of medical nanoparticles. *Taylor & FrancisE FröhlichInternational journal of nanomedicine, 2012•Taylor & Francis* **7**, 5577–5591 (2012).

49. Napolitano, G., Fasciolo, G. & Venditti, P. Mitochondrial management of reactive oxygen species. *Antioxidants* vol. 10 Preprint at https://doi.org/10.3390/antiox10111824 (2021).

50. Zhang, B. *et al.* Role of mitochondrial reactive oxygen species in homeostasis regulation. *Redox Report* vol. 27 Preprint at https://doi.org/10.1080/13510002.2022.2046423 (2022).

51. Rivas-García, L. *et al.* Ultra-small iron nanoparticles target mitochondria inducing autophagy, acting on mitochondrial dna and reducing respiration. *Pharmaceutics* **13**, (2021).

52. Dzeranov, A. *et al.* Iron Oxides Nanoparticles as Components of Ferroptosis-Inducing Systems: Screening of Potential Candidates. *Magnetochemistry* **9**, (2023).

53. Dietz, J. V., Fox, J. L. & Khalimonchuk, O. Down the iron path: Mitochondrial iron homeostasis and beyond. *Cells* vol. 10 Preprint at https://doi.org/10.3390/cells10092198 (2021).

54. Zhang, T. guang, Zhang, Y. long, Zhou, Q. qian, Wang, X. hui & Zhan, L. sheng. Impairment of mitochondrial dynamics involved in iron oxide nanoparticle-induced dysfunction of dendritic cells was alleviated by autophagy inhibitor 3-methyladenine. *Journal of Applied Toxicology* **40**, (2020).

55. Zhao, Y., Yang, M. & Liang, X. The role of mitochondria in iron overload-induced damage. *J. Transl. Med.* **22**, (2024).

56. Zhang, S. *et al.* Double-edge sword roles of iron in driving energy production versus instigating ferroptosis. *Cell Death and Disease* vol. 13 Preprint at https://doi.org/10.1038/s41419-021-04490-1 (2022).